Scalar Filtered Mass Density Function for Variable-Density Flows

POLITECNICO DI TORINO

SCUOLA DI DOTTORATO
Corso di dottorato in Fluidodinamica – XXIII ciclo

Tesi di Dottorato

Scalar Filtered Mass Density Function for Variable-Density Flows

Pietro Ferrero

Tutore
Prof. Domenic D'Ambrosio

Coordinatore del corso di dottorato
Prof. Gaetano Iuso

Gennaio 2012

Contents

Summary

Una metodologia denominata Scalar Mass Filtered Density Function (SFMDF) e' stata utilizzata per condurre Large Eddy Simulation (LES) di flussi turbolenti con reazioni chimiche. La SFMDF descrive la distribuzione delle fluttuazioni di sottoscala delle concentrazioni delle specie chimiche e dell'entalpia. Il grande vantaggio della formulazione SFMDF risiede nel fatto che il termine sorgente che descrive l'effetto delle reazioni chimiche appare in forma chiusa e non deve essere modellato. Il metodo presentato in questa tesi di dottorato si basa sull'equazione di trasporto della SFMDF, che viene risolta con un metodo Monte Carlo. La SFMDF e' in grado di fornire solo la concentrazione delle specie chimiche e l'entalpia: tutte le altre variabili devono essere calcolate da un solutore fluidodinamico. Questo tipo di approccio viene detto ibrido. Per questa tesi e' stato sviluppato un solutore Monte Carlo in grado di risolvere l'equazione di trasporto della SFMDF in forma Lagrangiana. Questo codice e' stato accoppiato a un codice fluidodinamico ai volumi finiti che opera su domini non strutturati sviluppato dalla University of Minnesota. I risultati dei test effettuati su mixing layer bi- e tri-dimensionali e su scie planari tridimensionali mostrano che il metodo e' consistente e accurato.

Chapter 1

Introduction

Turbulent reacting flows are of primary importance in many industrial processes as well as in transportation. They are also very challenging to simulate computationally due to the wide range of scales involved at high Reynolds number and the presence of stiff non-linear chemical terms.
At the moment, three major approaches exist for the simulation of such flows: Reynolds Averaged Navier Stokes (RANS), Large Eddy Simulation (LES) and Direct Numerical Simulation (DNS) [1], [2]. In RANS simulations only the time averaged form of the Navier-Stokes equations are explicitly solved, while all the fluctuating terms due to turbulence are modelled. That enables RANS simulations to provide solutions in "reasonable" time even for very large and complex domains and, for this reason, it is the only simulation strategy that is widely used in the industry. The biggest limitation of RANS lie in the fact that, even for non reacting flows, there are not universal models for the fluctuating terms and those available need to be constantly adjusted to fit experimental data. There are also known cases where RANS simulation are known to fail completely.
On the other side of the spectrum lies Direct Numerical Simulations, where all the fluid and chemical scales are explicitly computed and no modelling is required. For the time being (as well as for the foreseeable future), DNS simulations will be confined in academia and research labs, mainly because their computational cost which limits them to low Reynolds number flows. Despite these limitations, DNS is very useful for turbulence research and for the validations of closure models.
Large Eddy Simulation (LES) lies somewhere in between those two methodologies. The main idea behind LES simulations is to resolve all the large turbulent energy containing scales and to model only the dissipative ones. This achieved by passing the transport variables through a spatial filter and only solve for these ones. In doing so the effects of fluctuations at small (or unresolved) scales has to be modelled. These sub-grid scale (SGS) fluctuations are more universal and much less problem-dependent than those that has to be modelled for RANS [2]. Although LES is much more expensive than RANS methods, its superior accuracy has been widely demonstrated.
In the past two decades there have been significant advances for LES of turbulent flows. Comparatively not as much effort has been directed towards LES of chemically reacting

flows and even less for high-speed turbulent reactive flows. The main difficulty associated with a Large Eddy Simulation of turbulent reactive flows is the closure of the chemical source terms. Unlike the corresponding convective term, the chemical source term is far from being universal because it depends on the chemical kinetics involved, which is highly non-linear. Due to the lack of universal models in the literature, in most high speed LES simulations the influence of the turbulent scales on the source term is usually ignored [3]. The validity of this assumption has never been tested and, due to the complexities of the turbulence-reaction interaction, it seems questionable [4]. Even in low speed turbulent flows it has been demonstrated that neglecting the SGS contribution to the chemical source term can lead to incorrect results [14], [16].

Some of the most promising models for LES of turbulent reacting flows are those developed based on the solution of the SGS probability density function (PDF), termed the filtered density function (FDF). In this approach, the joint statistics of turbulent variables at the subgrid level are obtained from the transport equation for the single-point joint FDFs of these variables. All terms involving single-point statistics, e.g. the chemical source terms, appear in a closed form in the FDF equation, regardless of their complexity. This is the main advantage of the FDF method. However, the single-point FDF equation is not closed, and some form of modelling for multipoint correlations is needed. The FDF was formally derived by Pope [5] and the first implementation of this technique was made by Madnia and Givi [6]. Colucci [14] derived the FDF transport equation for constant-density flows and solved it with a Monte Carlo (MC) method. The same technique was used by Jaberi [16] to solve for the Scalar Filtered Mass Density Function (SFMDF), which is the extension of the FDF to variable-density flows. Both these models only focus on the probability density function (PDF) of the SGS fluctuations of the species mass fractions and the static enthalpy (hence the name scalar). The remaining flow quantities are computed by a conventional fluid dynamic solver in a hybrid fashion. This methodology was extended to the velocity-scalar and velocity-scalar-frequency FMDF later on. Although these latter formulations are more rigorous from a statistical/mathematical standpoint, they are much more computationally demanding. Furthermore, in all the previous applications of the LES/FDF approach, the effect of pressure on the scalar FMDF or the velocity-scalar-frequency FMDF was not considered. This effect can be ignored at low-Mach-number flows or constant pressure combustion but it should be included when dealing with a compressible flow. The only attempt that we know of including the pressure contribution is from Banaeizadeh et al. [15]. In this work we follow their approach.

In addition, most of the work done on LES-FMDF so far, with the only exception of Ansari [17], has been carried out on structured mesh and, therefore, has been limited to simple geometric configurations. The objective of this work is to use the compressible SFMDF methodology in conjunction with a high-order, unstructured compressible finite volume fluid solver (called US3D) in order to investigate high speed flows on non-trivial geometries. This requires to develop a Lagrangian Monte Carlo code to solve for the SFMDF transport equation and to couple it with US3D.

In chapter 2 the mathematical formulation of LES and the SFMDF is presented and the SFMDF transport equation is derived. All terms that needs modelling are discussed in detail. A possible extension of the SFMDF method for high-speed compressible flows is

also presented.
Chapter 3 gives a brief introduction of US3D and then describes in detail the Lagrangian Monte Carlo procedure that is used to solve the SFMDF transport equation and how it is coupled to US3D.
Chapter 4 show the consistency tests obtained on a three-dimensional and on a two-dimensional non-reactive temporal mixing layers and on a three-dimensional planar wake. Both variable-density and compressible flows are investigated and the SFMDF solutions are found to agree very well with those obtained form US3D.
Finally Chapter 5 summarizes what we accomplished and gives some suggestions on how to continue this work.

Chapter 2

Mathematical Formulation

In this chapter we introduce the set of Filtered Navier-Stokes equations that govern the dynamics of the flow field and highlight the unclosed terms that require filtering. Particular emphasis is placed on the chemical source term, as this is the object of the SFMDF approach.
Non-equilibrium conditions that are typical of high enthalpy fluid flows are not considered here, and thus our analysis will be restricted on subsonic or low supersonic flows.

2.1 Governing Equations

We consider a compressible turbulent flow involving N_s reacting species. For the mathematical description of this flow in a three-dimensional domain we need N_s species mass fraction conservation equations, three momentum conservation equations, an equation of state and an equation for the conservation of energy. For compressible flows different forms of the "energy" equation can be used. In this work we solve the total (internal + kinetic) energy equation, which has the desirable feature of being a conserved quantity. The governing equations are:

$$\frac{\partial}{\partial t}\left(\rho Y_s\right) + \frac{\partial}{\partial x_j}\left(\rho u_j Y_s\right) = -\frac{J_j^s}{\partial x_j} + \rho S_s, \qquad s = 1,2,...,N_s \tag{2.1a}$$

$$\frac{\partial}{\partial t}\left(\rho u_i\right) + \frac{\partial}{\partial x_j}\left(\rho u_i u_j\right) = \frac{\partial p}{\partial x_i} + \frac{\partial \tau_{ij}}{\partial x_j}, \tag{2.1b}$$

$$\frac{\partial}{\partial t}\left(\rho E\right) + \frac{\partial}{\partial x_j}\left[(\rho E + p)u_j\right] = \frac{\partial}{\partial x_j}\left(\tau_{ij} u_i\right) - \frac{\partial q_j}{\partial x_j} \tag{2.1c}$$

where u_i is the velocity vector, p the pressure, T the temperature, ρ the total density of the mixture, E the total energy per unit mass, while Y_s and S_s are the mass fraction $\left(\sum_{\alpha=1}^{N_s} Y_\alpha = 1\right)$ and the chemical source term of species s, respectively. By summing Eq. 2.1a over all the N_s species, the terms of the right hand side sum identically to zero and we recover the traditional continuity equation:

$$\frac{\partial \rho}{\partial t} + \frac{\partial \rho u_j}{\partial x_j} = 0 \tag{2.2}$$

The perfect gas law is used as the equation of state:

$$p = \rho \overline{R} T \sum_{s=1}^{N_s} Y_s / M_s = \rho R T \tag{2.3}$$

where $\overline{R}$ is the universal gas constant and M_s is the molecular weight of species s.
In lieu of Eq. 2.1c, a static enthalpy equation can be also be used

$$\frac{\partial}{\partial t}(\rho h) + \frac{\partial}{\partial x_j}(\rho h u_j) = -\frac{\partial q_j}{\partial x_j} + \tau_{ij}\frac{\partial u_i}{\partial x_j} \tag{2.4}$$

The static enthalpy of the mixture is defined as

$$h = \sum_{s=1}^{N_s} h_s Y_s \tag{2.5}$$

and the species static enthalpy is

$$h_s = \int_{T_0}^{T} C_{p_s} dT + \Delta h^0_{f,s}, \tag{2.6}$$

where $\Delta h^0_{f,s}$ and C_{p_s} are the enthalpy of formation and the specific heat at constant pressure of species s, respectively. The reference temperature T_0 is set to 0 K.

2.1.1 Diffusive Terms

For a Newtonian fluid the viscous momentum stresses are represented by

$$\tau_{ij} = \mu\left(\frac{\partial u_i}{\partial x_j} + \frac{\partial u_j}{\partial x_i} - \frac{2}{3}\frac{\partial u_k}{\partial x_k}\delta ij\right), \tag{2.7}$$

and the mass viscous flux depends on the diffusion velocity ($v_{i,s}$) of species s:

$$J_j{}^s = \rho Y_s v_{i,s}. \tag{2.8}$$

The energy flux q_j is

$$q_j = -k\frac{\partial T}{\partial x_j} + \rho \sum_{s=1}^{N_s} Y_s h_s v_{j,s} \tag{2.9}$$

The first term represents heat diffusion and is expressed by Fourier's law, where λ is the thermal conductivity of the mixture. The second term is associated with diffusion of species with different enthalpies and it is present only in multi-species mixtures. The diffusion velocities are in general a function of gradients of concentrations, temperature

and pressure. In this work we neglect the temperature and pressure effects and model the mass viscous flux only based on the gradients of concentration through the Fick's law:

$$J_j{}^s = \rho Y_s v_{i,s} = -\rho D_s \frac{\partial Y_s}{\partial x_j} \tag{2.10}$$

where differential mass diffusion is neglected by replacing the multicomponent diffusion coefficients with a single binary diffusion coefficient D.
The final form of the mass and energy viscous fluxes are

$$J_j{}^s = -\rho D \frac{\partial Y_s}{\partial x_j} \tag{2.11}$$

$$q_j = -k\frac{\partial T}{\partial x_j} + \rho \sum_{s=1}^{N_s} h_s D \frac{\partial Y_s}{\partial x_j} \tag{2.12}$$

Assuming a constant C_p, Eq. 2.12 can also be written as

$$q_j = -\rho \nu_{th} \frac{\partial h}{\partial x_j} + \rho \sum_{s=1}^{N_s} h_s D \frac{\partial Y_s}{\partial x_j} \tag{2.13}$$

where the thermal diffusivity is defined as $\nu_{th} = \frac{k}{\rho C_p}$.

2.1.2 Low Mach Number Approximation

In the case a low Mach number flow the total derivative of the pressure and the viscous dissipation term in the static enthalpy equation (Eq. 2.4) become negligible [1] and the simplified enthalpy equation

$$\frac{\partial \rho h}{\partial t} + \frac{\partial \rho h u_j}{\partial x_j} = -\frac{\partial J_j^h}{\partial x_j} \tag{2.14}$$

has the same form of the scalar mass fraction equations (Eq. 2.1a). In this special case, we can write Eqs. 2.1a and Eq. 2.14 in a compact form as

$$\frac{\partial \rho \phi_\alpha}{\partial t} + \frac{\partial \rho u_j \phi_\alpha}{\partial x_j} = -\frac{\partial J_j^\alpha}{\partial x_j} + \rho S_\alpha, \qquad \alpha = 1,2,...,N_s+1 \tag{2.15}$$

where $\phi_{\alpha=1,2,...,N_s}$ are the N_s species mass fraction and $\phi_{\alpha=N_s+1}$ is the specific enthalphy. The source terms are

$$S_\alpha = \begin{cases} \dot{\omega}_\alpha & \text{for } \alpha = 1,...,N_s \\ 0 & \text{for } \alpha = N_s+1 \end{cases} \tag{2.16}$$

Furthermore, if we assume that the Schmidt and the Prandtl number are the same ($Le = 1$) and we neglect the diffusion of species with different enthalpies, Eq. 2.11 and 2.12 can be grouped together as

$$J_j{}^\alpha = -\gamma \frac{\partial \phi_\alpha}{\partial x_j}, \;\; \alpha = 1,...,N_s+1 \tag{2.17}$$

where $\gamma = \rho\Gamma$ represents the mass and the thermal diffusivities.

2.2 Large Eddy Simulation Equations

In Large Eddy simulation the spatial filtering operation

$$\langle Q\left(\mathbf{x},t\right)\rangle_{\ell} = \int_{\mathcal{D}} Q(\mathbf{x'},t)G(\mathbf{x'},\mathbf{x})d\mathbf{x'} \tag{2.18}$$

is applied to all the flow variables in order to remove the small scale fluctuations and only retain the energy containing eddies. In the previous equation, $G(\mathbf{x'},\mathbf{x})$ represents the filter function, $\mathcal{D}$ is the computational domain, while $Q\left(\mathbf{x},t\right)$ is the generic transport variable, which is a function of space and time. We consider a filter function that is spatially and temporally invariant and localized, i.e. $G(\mathbf{x'},\mathbf{x}) = G(\mathbf{x'}-\mathbf{x})$, with the properties $G(\mathbf{x}) > 0$ and $\int_{\mathcal{D}} G(\mathbf{x})d\mathbf{x} = 1$.
In variable-density flows it is convenient to use the Favre averaging

$$\langle Q\left(\mathbf{x},t\right)\rangle_{L} = \frac{\langle \rho Q\rangle_{\ell}}{\langle \rho\rangle_{\ell}}, \tag{2.19}$$

so that the continuity equation remains unchanged after the filtering.
The filtered forms of Eqs. 2.1 are

$$\frac{\partial \langle\rho\rangle_{\ell}\langle Y_s\rangle_{L}}{\partial t} + \frac{\partial \langle\rho\rangle_{\ell}\langle Y_s\rangle_{L}\langle u_j\rangle_{L}}{\partial x_j} + \frac{\partial \langle J_j{}^{s}\rangle_{\ell}}{\partial x_j} = -\frac{M_j^s}{\partial x_j} + \langle \rho S_s\rangle_{\ell} \tag{2.20a}$$

$$\frac{\partial \langle\rho\rangle_{\ell}\langle u_i\rangle_{L}}{\partial t} + \frac{\partial \langle\rho\rangle_{\ell}\langle u_i\rangle_{L}\langle u_j\rangle_{L}}{\partial x_j} - \frac{\partial \langle p\rangle_{\ell}}{\partial x_i} - \frac{\partial \langle\tau_{ij}\rangle_{L}}{\partial x_j} = -\frac{\partial T_{ij}}{\partial x_j} \tag{2.20b}$$

$$\frac{\partial \langle\rho\rangle_{\ell}\langle E\rangle_{L}}{\partial t} + \frac{\partial}{\partial x_j}\left[\langle\rho\rangle_{\ell}\langle E\rangle_{L}\langle u_j\rangle_{L} + \langle q_j\rangle_{L} - \langle\tau_{ij}\rangle_{L}\langle u_i\rangle_{L}\right] = -\frac{\partial}{\partial x_j}\left(C_p Q_j + \frac{1}{2}S_j - D_j\right) \tag{2.20c}$$

The effect of the Sub Grid Scales (SGS) terms appear on the left hand side and need to be modelled. These are the SGS stresses T_{ij}, the SGS mass flux M_i^s, the SGS heat flux Q_j, the SGS turbulent diffusion $\partial S_j/\partial x_j$, the SGS viscous diffusion D_j and the chemical source term $\langle \rho S_s\rangle_{\ell}$. They are defined as

$$T_{ij} = \langle\rho\rangle_{\ell}\left(\langle u_i u_j\rangle_{L} - \langle u_i\rangle_{L}\langle u_j\rangle_{L}\right) \tag{2.21a}$$

$$M_j^s = \langle\rho\rangle_{\ell}\left(\langle Y_s u_j\rangle_{L} - \langle Y_s\rangle_{L}\langle u_j\rangle_{L}\right) \tag{2.21b}$$

$$Q_j = \langle\rho\rangle_{\ell}\left(\langle T u_j\rangle_{L} - \langle T\rangle_{L}\langle u_j\rangle_{L}\right) \tag{2.21c}$$

$$S_j = \langle\rho\rangle_{\ell}\left(\langle u_k u_k u_j\rangle_{L} - \langle u_k u_k\rangle_{L}\langle u_j\rangle_{L}\right) \tag{2.21d}$$

$$D_j = \langle\tau_{ij} u_i\rangle_{\ell} - \langle\tau_{ij}\rangle_{L}\langle u_i\rangle_{L} \tag{2.21e}$$

Furthermore, in a conventional LES for reactive flows, the chemical source term is usually modeled as

$$\langle S_{\alpha}(\phi_{\alpha})\rangle_{L} = S(\langle\phi_{\alpha}\rangle_{L}) \tag{2.22}$$

which means that the SGS effects are completely neglected. In the Scalar Filtered Mass Fraction methodology (SFMDF), on the other hand, the chemical source terms appear in closed form and no modelling is required.

2.2.1 Model of the SGS quantities

For low Mach number flows the SGS closure problem is associated with the SGS stresses T_{ij}, the SGS mass flux M_i^α and the chemical source term $\langle \rho S_s \rangle_\ell$. For compressible flows, when the total energy equation is used, also the SGS heat flux, the SGS turbulent diffusion and the SGS viscous diffusion are unclosed and requires modelling.
The Sub Grid Scale stresses (Eq. 2.21a) are closed using an Eddy-Viscosity model.

$$T_{ij} = -2\rho\nu_T \left(\langle S_{ij} \rangle_L - \frac{1}{3} \langle S_{kk} \rangle_L \delta_{ij} \right) \tag{2.23}$$

where $S_{ij} = \frac{1}{2}(\partial u_i/\partial x_j + \partial u_j/\partial x_i)$ is the rate of strain tensor and ν_T is the Eddy viscosity. The idea behind eddy-viscosity models is to try to reproduce the exchange of energy between the resolved and the unresolved scales by mimicking the drain of energy that characterizes the turbulent cascade. The SGS mass and heat transfer fluxes are also treated using an Eddy-diffusivity approach [7]

$$M_j^s = -\frac{\rho\nu_T}{Sc_T} \frac{\partial \langle Y_s \rangle}{\partial x_j} \tag{2.24}$$

$$Q_j = -\frac{\rho\nu_T}{Pr_T} \frac{\partial \langle T \rangle}{\partial x_j} \tag{2.25}$$

in which the turbulent Schmidt and Prandtl numbers are constants of the model. No attempt is done to evaluate them dynamically, although some dynamical models have been shown to give better results [8]. Note that if $Pr_T = Sc_T$ and the specific heats are constant, the previous equations can be written in a compact form as

$$R_j^\alpha = -\rho\gamma_T \frac{\partial \langle \phi_\alpha \rangle}{\partial x_j} \tag{2.26}$$

where $\gamma_T = \langle \rho \rangle_\ell \Gamma_T$, $\Gamma_T = \nu_T/Sc_T = \nu_T/Pr_T$ and ϕ_α is the scalar vector that contains the N_s species mass fraction plus static enthalpy (Cfr. Sec. 2.1.2).

The calculation of the Eddy-Viscosity is a central problem in LES and over the years many different models have been proposed. In this thesis we used two different models, the Modified Kinetic Energy Model and the Spalart-Allmaras Model. The former is a modified, compressible version of the one proposed by Bardina et al. [10] in which the sub-grid viscosity is determined based on the modified subgrid kinetic energy

$$\nu_T = C_k \Delta_G \sqrt{|\langle u_i^* \rangle_L \langle u_i^* \rangle_L - \langle \langle u_i^* \rangle_L \rangle_{L'} \langle \langle u_i^* \rangle_L \rangle_{L'}|} \tag{2.27}$$

where $u_i^* = u_i - \mathcal{U}_i$ and $\mathcal{U}_i$ is a reference velocity which is imposed to guarantee the Galilean invariance of the model. The subscript L' denotes the filter at the secondary level which has a characteristic filter width larger than that of the grid level filter (Δ_L). The MKEV model has been used by several authors and has been shown to give better performances than the static Smagorinsky model.

The second model employed in this work is the Spalart-Allmaras model (SA) [11]. Originally developed for Raynolds Averaged Navier Stoked (RANS) closures, the SA model has been recently adapted to Detached-Eddy Simulations (DES) and has provided good results in this configuration. The SA model determines the Eddy-Viscosity by solving a semi-empirical transport equation for ν_T and, although developed for wall-bounded flows, can also be applied to LES of free flows.
The SGS turbulent diffusion is modeled following Knight et Al. [9].

$$S_j = \langle u_k \rangle_L T_{jk} \tag{2.28}$$

where T_{jk} is given by 2.23.
No attempt is made to model the SGS viscous diffusion (D_j), as no models are currently available in the literature and because its relative importance compared to the other SGS terms in the total energy equation is negligible [8].

2.3 Scalar Filtered Mass Density Function (SFMDF) for low Mach number flows

The object of the Scalar Filtered Mass Density Function (SFMDF) methodology is to provide an exact expression for the chemical source term, without resorting to modelling as it is done in conventional LES (Eq. 2.22). To achieve this goal, the scalar fluctuations of the scalar array (the N_s species mass fraction plus enthalpy) are considered in a probabilistic manner.
In this section we will be describing the formulation for Low Mach number flows (Sec. 2.1.2). A proposed extension to take compressibility into account will be given in a later section.
Jaberi [16] defined the Scalar Filtered Mass Density Function ($\mathcal{F}_L$) as

$$\mathcal{F}_L(\Psi;\mathbf{x},t) = \int_{-\infty}^{+\infty} \rho(\mathbf{x'},t)\sigma[\Psi,\Phi(\mathbf{x'},t)]G(\mathbf{x'}-\mathbf{x})d\mathbf{x'} \tag{2.29}$$

where the fine-grained density [12] is defined as

$$\sigma[\Psi,\Phi(\mathbf{x'},t)] = \prod_{\alpha=1}^{N_s+1} \delta(\psi_\alpha - \phi_\alpha(\mathbf{x},t)). \tag{2.30}$$

with G being the LES filter function introduced in Eq. 2.18, δ is the Dirac delta function and Ψ is the vector of the scalars in the sample space. The SFMDF is the extension for variable-density flows of the Filtered Density Function (FDF), originally introduced by Pope [5]. Eq. 2.29 also implies that the SFMDF is the mass density spatially filtered value of the fine-grained density. In fact, by integrating over all composition domain

$$\int_{-\infty}^{+\infty} \mathcal{F}_L(\Psi;\mathbf{x},t)d\Psi = \int_{-\infty}^{+\infty} \rho(\mathbf{x'},t)G(\mathbf{x'}-\mathbf{x})d\mathbf{x'} = \langle \rho(\mathbf{x},t) \rangle_\ell \,, \tag{2.31}$$

the filtered density is recovered.
The conditional filtered average of any variable Q is defined as

$$\langle Q(\mathbf{x},t)|\Psi\rangle_L = \frac{1}{\mathcal{F}_L}\int_{-\infty}^{+\infty}\rho(\mathbf{x'},t)Q(\mathbf{x'},t)\sigma[\Psi,\Phi(\mathbf{x'},t)]G(\mathbf{x'}-\mathbf{x})d\mathbf{x'}. \tag{2.32}$$

Following directly from Eq. 2.32:

1. For $Q(\mathbf{x},t)=c$, where c is a constant:

$$\langle Q(\mathbf{x},t)|\Psi\rangle_L = c \tag{2.33}$$

2. For $Q(\mathbf{x},t)=\hat{Q}(\phi(\mathbf{x},t))$, where $\hat{Q}$ is a variable that can completely described by compositional vector $\phi(\mathbf{x},t)=[\phi_1,\phi_2,...,\phi_{N_s+1}]$:

$$\langle Q(\mathbf{x},t)|\Psi\rangle_L = \hat{Q}(\psi) \tag{2.34}$$

3. Integral property:

$$\int_{-\infty}^{+\infty}\langle Q(\mathbf{x},t)|\Psi\rangle_L \mathcal{F}_L(\Psi;\mathbf{x},t)d\Psi = \langle\rho(\mathbf{x},t)\rangle_\ell \langle Q(\mathbf{x},t)\rangle_L \tag{2.35}$$

From this properties it follows that the filtered value of any function of the scalar variables (i.e. the chemical source term) is obtained by integration over the composition space.
The SMFDF transport equation is

$$\frac{\partial\mathcal{F}_L}{\partial t}+\frac{\partial\left[\langle u_j|\psi\rangle_\ell\mathcal{F}_L\right]}{\partial x_j}=\frac{\partial}{\partial\psi_\alpha}\left[\left\langle\frac{1}{\hat{\rho}(\phi)}\frac{J_j^\alpha}{\partial x_j}|\psi\right\rangle_\ell\mathcal{F}_L\right]-\frac{\partial}{\partial\psi_\alpha}\left[\hat{S}_\alpha(\psi)\mathcal{F}_L\right] \tag{2.36}$$

where the conditional filtered averages terms (convection and mixing) involve two-points correlations and must be modelled. The convection term is decomposed as

$$\langle u_j|\psi\rangle_\ell\mathcal{F}_L=\langle u_j\rangle_L\mathcal{F}_L+\left[\langle u_i|\psi\rangle_\ell-\langle u_i\rangle_L\right]\mathcal{F}_L, \tag{2.37}$$

while the mixing term, using Fick's law and the assumption of constant molecular diffusion [12], becomes

$$\frac{\partial}{\partial\psi_\alpha}\left[\left\langle\frac{1}{\hat{\rho}(\phi)}\frac{\partial}{\partial x_i}\gamma\frac{\partial\phi_\alpha}{\partial x_i}|\psi\right\rangle_\ell\mathcal{F}_L\right]=\frac{\partial}{\partial x_i}\left(\gamma\frac{\partial(\mathcal{F}_L/\hat{\rho})}{\partial x_i}\right)-\frac{\partial^2}{\partial\psi_\alpha\psi_\beta}\left[\left\langle\gamma\frac{\partial\phi_\alpha}{\partial x_i}\frac{\partial\phi_\beta}{\partial x_i}\right\rangle_\ell\mathcal{F}_L/\hat{\rho}\right] \tag{2.38}$$

By substituting Eq. 2.37 and Eq. 2.38 into 2.36, we get

$$\begin{aligned}\frac{\partial\mathcal{F}_L}{\partial t}=&-\frac{\partial\left[\langle u_j|\psi\rangle_\ell\mathcal{F}_L\right]}{\partial x_j}-\frac{\partial}{\partial x_i}\left(\gamma\frac{\partial(\mathcal{F}_L/\hat{\rho})}{\partial x_i}\right)-\frac{\partial^2}{\partial\psi_\alpha\psi_\beta}\left[\left\langle\gamma\frac{\partial\phi_\alpha}{\partial x_i}\frac{\partial\phi_\beta}{\partial x_i}\right\rangle_\ell\mathcal{F}_L/\hat{\rho}\right]\\&-\frac{\partial\left[\langle u_i|\psi\rangle_\ell-\langle u_i\rangle_L\right]\mathcal{F}_L}{\partial x_i}-\frac{\partial}{\partial\psi_\alpha}\left[\hat{S}_\alpha(\psi)\mathcal{F}_L\right]\end{aligned} \tag{2.39}$$

This equation is still an exact transport equation for the SMFDF. The first and second terms on the right-hand side represent convection and diffusion in physical space, respectively, and they are closed. The last term on the right-hand side is the chemical source term and it is also closed. The unclosed terms are the third one and the fourth one on the right-hand side and they represent the effects of SGS mixing and convection, respectively. The convection term is modelled adopting a gradient diffusion hypothesis:

$$\left[\langle u_i|\psi\rangle_\ell - \langle u_i\rangle_L\right]\mathcal{F}_L = -\gamma_T \frac{\partial(\mathcal{F}_L/\langle\rho\rangle_\ell)}{\partial x_i} \tag{2.40}$$

The advantage of this choice is that the first moment of Eq. 2.40,

$$\langle\rho\rangle_\ell \left[\langle u_i\phi_\alpha\rangle_L - \langle u_i\rangle_L \langle\phi_\alpha\rangle_L\right] = -\gamma_T \frac{\partial \langle\phi_\alpha\rangle_L}{\partial x_i} \tag{2.41}$$

is identical to the SGS closure adopted in conventional LES (Eq. 2.26).
The closure adopted for the mixing term is based on the Interaction by Exchange with the Mean model (IEM):

$$\frac{\partial^2}{\partial\psi_\alpha\psi_\beta}\left[\left\langle \gamma \frac{\partial\phi_\alpha}{\partial x_i}\frac{\partial\phi_\beta}{\partial x_i}\right\rangle_\ell \mathcal{F}_L/\hat{\rho}\right] = -\frac{\partial}{\partial\psi_\alpha}\left[\Omega_m(\psi_\alpha - \langle\phi_\alpha\rangle_L)\mathcal{F}_L\right] \tag{2.42}$$

where Ω_m is the SGS mixing frequency and it is modelled as

$$\Omega_m(\mathbf{x},t) = \frac{C_\Omega(\gamma+\gamma_T)}{\langle\rho\rangle_\ell \Delta_G^2} \tag{2.43}$$

where Δ_G is the filter width.
To establish consistency between the SMFDF and conventional moment closure, an additional minor assumption is made

$$\frac{\partial}{\partial x_i}\left(\gamma\frac{\partial(\mathcal{F}_L/\hat{\rho})}{\partial x_i}\right) \approx \frac{\partial}{\partial x_i}\left(\gamma\frac{\partial(\mathcal{F}_L/\langle\rho\rangle_\ell)}{\partial x_i}\right). \tag{2.44}$$

With this assumption and the closures given by Eq. 2.40 and 2.42, the modeled SFMDF transport equation is

$$\begin{aligned}\frac{\partial\mathcal{F}_L}{\partial t} + \frac{\partial\left[\langle u_j|\psi\rangle_\ell \mathcal{F}_L\right]}{\partial x_j} = &-\frac{\partial}{\partial x_i}\left(\gamma\frac{\partial(\mathcal{F}_L/\langle\rho\rangle_\ell)}{\partial x_i}\right) + \frac{\partial}{\partial\psi_\alpha}\left[\Omega_m(\psi_\alpha - \langle\phi_\alpha\rangle_L)\mathcal{F}_L\right] \\ &- \gamma_T\frac{\partial(\mathcal{F}_L/\langle\rho\rangle_\ell)}{\partial x_i} - \frac{\partial}{\partial\psi_\alpha}\left[\hat{S}_\alpha(\psi)\mathcal{F}_L\right]\end{aligned} \tag{2.45}$$

The first and second moments of Eq. 2.45 are, respectively,

$$\frac{\partial\langle\rho\rangle_\ell\langle\phi_\alpha\rangle_L}{\partial t} + \frac{\partial\langle\rho\rangle_\ell\langle\phi_\alpha\rangle_L\langle u_j\rangle_L}{\partial x_j} = \frac{\partial}{\partial x_j}\left[(\gamma+\gamma_T)\frac{\partial\langle\phi_\alpha\rangle_L}{\partial x_j}\right] + \langle\rho S_\alpha\rangle_\ell \tag{2.46}$$

$$\begin{aligned}\frac{\partial\langle\rho\rangle_\ell\sigma_\alpha^2}{\partial t} + \frac{\partial\langle\rho\rangle_\ell\sigma_\alpha^2\langle u_j\rangle_L}{\partial x_j} = &\frac{\partial}{\partial x_j}\left[(\gamma+\gamma_T)\frac{\partial\sigma_\alpha^2}{\partial x_j}\right] + 2(\gamma+\gamma_T)\left[\frac{\partial\langle\phi_\alpha\rangle_L}{\partial x_j}\frac{\partial\langle\phi_\alpha\rangle_L}{\partial x_j}\right] \\ &- 2\Omega_m\langle\rho\rangle_\ell\sigma_\alpha^2 + 2(\langle\rho\phi_\alpha S_\alpha\rangle_\ell - (\langle\rho\rangle_L\langle\phi_\alpha\rangle_L\langle S_\alpha\rangle_L).\end{aligned} \tag{2.47}$$

where the SGS variance is defined as $\sigma_\alpha^2 = \langle \phi_\alpha^2 \rangle_L - \langle \phi_\alpha \rangle_L^2$. The equation for the first moment (Eq. 2.46) can be obtained by directly filtering Eq. 2.15 and adopting the SGS closure of Eq. 2.41. Eq. 2.46 and 2.47 can be solved using a conventional finite volume or finite difference method and this redundancy provides a good test to check the consistency of the SFMDF formulation.

2.4 Monte Carlo Solution of the SFMDF

Due to the high dimensionality of the SMFDF transport equation (Eq. 2.45), conventional numerical methods to solve it, e.g. finite difference or finite volume, are computationally very expensive and impractical. Instead, a Lagrangian Monte Carlo procedure [12] is employed; the Lagrangian formulation, although a little more complex to implement on unstructured grids, is known to give much more accurate results with the respect to the Eulerian one [13].
The domain is filled with Monte Carlo elements (stochastic particles) which move in space because of convection - due to the mean filtered velocity - and because of molecular and sub-grid diffusion. In addition, the particles can change their composition because of mixing and chemical reactions.
The physical motion is governed by the general diffusion process

$$dX_i = D_i(X(t),t)dt + E(X(t),t)dW_i \tag{2.48}$$

where X_i is the Lagrangian position of the particle, D_i and E are the drift and diffusion coefficients, respectively, and dW_i denotes the Wiener-Levy process. These coefficient are derived by comparing the Fokker-Planck equation corresponding to Eq. 2.48 with the spatial derivative terms in the SFMDF transport equation (Eq. 2.45):

$$D_i(X(t),t) = \langle u_i \rangle_L + \frac{1}{\langle \rho \rangle_\ell} \frac{\partial(\gamma + \gamma_T)}{\partial x_i}; \qquad E(X(t),t) = \sqrt{\frac{2(\gamma + \gamma_T)}{\langle \rho \rangle_L}} \tag{2.49}$$

The subgrid mixing and chemical reaction term are implemented by altering the composition of the particles

$$\frac{d\phi_\alpha^+}{dt} = -\Omega_m(\phi_\alpha^+ - \langle \phi_\alpha \rangle_L) + \hat{S}_\alpha(\phi_\alpha^+) \tag{2.50}$$

where ϕ_α^+ denotes the scalar value of the particle at the Lagrangian position X_i.
According to the principle of equivalent systems [12], the solutions of Eq. 2.48 and 2.50 yield the same statistics as solving directly the SMFDF transport equation (Eq. 2.45).

2.5 SFMDF for compressible flows

The methodology described in Sec. 2.3 assumes that the total pressure and the viscous dissipation terms in the static enthalpy equation (Eq. 2.4) are negligible and does not account for them. This simplified form of the enthalpy equation (Eq. 2.14) has the same mathematical form of the mass fraction equations and thus the SFMDF formulation can

be used for all the scalars ϕ_α involved in the simulation (N_s species mass fractions and enthalpy). In the case of a compressible high Mach number flow, the total pressure and the viscous dissipations terms cannot be neglected and must be included in the formulation [15]. This can be achieved by including these two contributions in the source term of the enthalpy equation. The mass fraction/enthalpy equation is unchanged (Eq. 2.15):

$$\frac{\partial \rho \phi_\alpha}{\partial t} + \frac{\partial \rho u_j \phi_\alpha}{\partial x_j} = -\frac{\partial J_j^\alpha}{\partial x_j} + \rho S_\alpha, \qquad \alpha = 1,2,...,N_s+1, \tag{2.51}$$

but now the source term S_α is

$$S_\alpha = \begin{cases} \dot{\omega}_\alpha & \text{for } \alpha = 1,...,N_s \\ \frac{1}{\rho}\left(\frac{\partial p}{\partial t} + u_i \frac{\partial p}{\partial x_i} + \tau_{ij}\frac{\partial u_i}{\partial x_j}\right) & \text{for } \alpha = N_s+1 \end{cases} \tag{2.52}$$

Eq. 2.51 and 2.52 are filtered and a procedure very similar to the one detailed in the previous section is employed to derive the SFMDF compressible tranport equation. This is the exact same as 2.45, with the addition of the conditional averages of the pressure and viscous dissipations terms. These are modelled as

$$\left\langle \left(\frac{1}{\rho}\frac{\partial p}{\partial t}\right) | \psi \right\rangle_\ell \mathcal{F}_L = \frac{1}{\langle \rho \rangle_\ell}\left(\frac{\partial \langle p \rangle_\ell}{\partial t}\right)\mathcal{F}_L, \tag{2.53}$$

$$\left\langle \left(\frac{1}{\rho} u_i \frac{\partial p}{\partial x_i}\right) | \psi \right\rangle_\ell \mathcal{F}_L = \frac{1}{\langle \rho \rangle_\ell}\langle u_i \rangle_\ell \frac{\partial \langle p \rangle_\ell}{\partial x_i}\mathcal{F}_L, \tag{2.54}$$

$$\left\langle \left(\frac{1}{\rho} \tau_{ij} \frac{\partial u_i}{\partial x_j}\right) | \psi \right\rangle_\ell \mathcal{F}_L = \frac{1}{\langle \rho \rangle_\ell}\langle \tau_{ij} \rangle_\ell \frac{\partial \langle u_i \rangle_\ell}{\partial x_j}\mathcal{F}_L, \tag{2.55}$$

In Eq. 2.53 to 2.55, the effect of the SGS pressure and viscous dissipation is neglected, although it may be significant in high speed flows. Further investigations are needed to assess the validity of these assumptions.

Chapter 3

Numerical Method

The numerical solution of the governing equations is based on a hybrid methodology in which the Favre-filtered Navier-Stokes equations (Eq. 2.20) are solved using a high-order Finite-Volume method, while the SFMDF transport eqution (Eq. 2.45) is solved using a Monte Carlo Lagrangian 'grid free' procedure. Fig. 3.1 shows the main features of this Hybrid Monte Carlo/Finite Volume (MC/FV) methodology. The FV solver is used

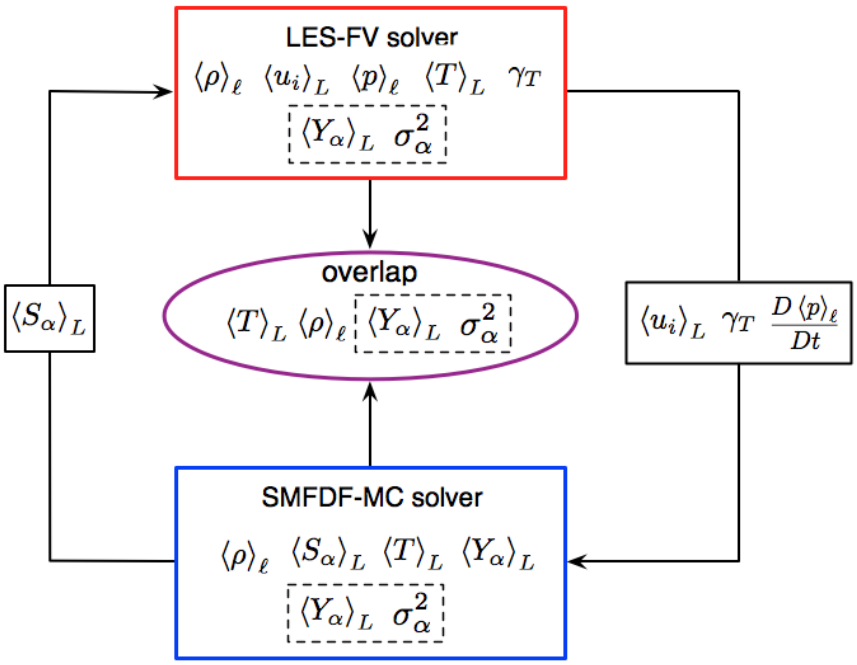

Figure 3.1. Diagram showing the basic coupling between the Finite Volume solver and the Monte Carlo solver.

to calculate the hydrodynamic variables, while the MC solver determines the scalar field

(species mass fraction and enthalpy) and the chemical source term. The MC solver receives from the FV solver the filtered velocity field, the Eddy-Viscosity field and, in the case of compressible flows, the total derivative of the pressure. It then feeds back to the FV solver the filtered chemical source term and the species mass fractions. Even in this "basic" coupling, both density and temperature fields are calculated by both solvers and this redundancy can be used for consistency checks. These tests can be further expanded by letting the finite volume scheme solve also for the first two moments of the SFMDF trasport equation (Eq. 2.46 and 2.47) and compare the overlapping species mass fractions ($\langle Y_\alpha \rangle_L$) and SGS variance ($\sigma_\alpha$) fields (dashed boxes in Fig. 3.1).
The FV solver employed for this work is US3D, a Three-Dimensional Unstructured Finite Volume code developed at the University of Minnesota. In addition a Parallel Monte Carlo solver with particle tracing capabilities was newly developed for this application and it was coupled to US3D.
The next section provides a brief description of the main features of US3D, while Sec. 3.2 characterizes more in depth the Monte Carlo procedure and how that was implemented on an unstructured code.

3.1 US3D Solver

US3D (UNstructured 3D) is a parallel implicit solver for the solution of the compressible Navier-Stokes equations with finite rate chemistry on unstructured finite volume meshes [19], [20]. Flow variables are stored at cell centers and the Navier-Stokes equations (2.1) are discretized in space by using the divergence theorem and write the rate of change of the conserved variable as the sum of fluxes over all faces of the cell

$$\frac{\partial \overline{U}}{\partial t} = -\frac{1}{V} \sum_{faces} \left[(\overrightarrow{F_c} - \overrightarrow{F_v}) \cdot \widehat{n} S \right] \tag{3.1}$$

where $\overline{U}$ denotes the average value of U inside the element, V is the volume of the element, $\widehat{n}$ is the unit outward-pointing normal, S is the face area and the summation is for every face of the element. The solver supports four types of element: tetrahedra, pyramids, prisms and hexahedra which are made of, respectively, of four, five, six and eight nodes.
The inviscid part of the fluxes are calculated using the modified Steger-Warming method [21], [22]. Alternatively, two high order methods can be utilized which are formally “4th” and “6th” order accurate on Cartesian mesh [23]. These high resolution schemes use the cell-centered gradient of the flow variables to build a higher order reconstruction of the flux. The caveat is that their performances are poorer if the neighbouring elements of a face are not aligned, as in the case of a mesh made of tetrahedra.
Both implicit and explicit time integration methods can be used by US3D.

3.1.1 Gradient reconstruction

The cell-centered gradients are used in the solver for the evaluation of the higher order inviscid fluxes as well as for the viscous ones. In addition, in the SFMDF scheme, the

velocity gradients are used to interpolate the cell-centered fluid velocity to the particle location.
The cell-centered gradients are computed using a least square (LS) fit, which can also be weighted using the inverse distance between elements [24]. Only the cell-centered data of the elements that share a face with the current element are included in the stencil. The LS method fits an hyperplane on all the data point that belong to the stencil by solving a linear system of equations at each element. In the absence of gird deformation, the linear operator can be calculated once, inverted and then stored at start-up. The LS fit is particularly suitable for unstructured grids.

3.2 Monte Carlo Solver

As described in Sec. 2.4, the SFMDF transport equation is solved using a Lagrangian "grid-free" Monte Carlo procedure, which employs stochastic particles that undergo motion in physical space and whose composition changes with time because of mixing and chemical reactions. The term "grid-free" refers to the fact that, in theory, no computational grid is required for the Monte Carlo solver, as the particles moves freely in space. In practice, some reference grid is required when statistical moments are calculated, as explained later in this section. For this purpose a different grid can be created for the MC solver or the grid used by the FV solver can be used. For this work we chose the latter solution, which has the advantages of requiring less memory and taking advantage of the fact that the FV grid is already clustered in regions of large gradients.
Numerically, a splitting operation is employed, in which transport in physical and composition spaces are treated separately.
At every time step, three main operations are performed:

1. Each particle is moved to a new position determined by the Stochastic Differential Equations (Eq. 2.48) . This step requires to track the particle on the unstructured grid and the algorithm used for this purpose is described in Sec. 3.2.2.

2. Ensemble averages are collected.

3. Particle composition is changed due to the mixing model and chemical reactions.

The simplest way of simulating the general diffusion process (Eq. 2.48) is through the Euler-Maruyamma approximation

$$X_i^{(n)}(t_{k+1}) = X_i^{(n)}(t_k) + D_i^{(n)}(t_k)\Delta t + E^{(n)}(t_k)(\Delta t)^{1/2}\xi^{(n)}(t_k) \tag{3.2}$$

where $\Delta t = t_{k+1} - t_k$ is the simulation time step and $D_i^{(n)}(t_k) = D_i(X_i^{(n)}(t),t)$ and $E^{(n)}(t_k) = E(X_i^{(n)}(t),t)$ are the drift and diffusion coefficients (Eq. 2.49) calculated at the particle location. $\xi^{(n)}$ is a random variable with a standard Gaussian PDF. Although simple, this formulation preserves the Markovian character of the diffusion process. Higher order schemes can be used but they must preserve the Ito-Gikhman nature of the process. The filtered velocities and turbulent fields that appear in the drift and diffusion coefficients

of Eq. 3.2 are interpoled to the particle position using the gradients that are available at the cell center:

$$\theta_p = \theta_i + (\nabla\theta)_i \cdot (\mathbf{r}_i - \mathbf{r}_p) \tag{3.3}$$

where θ is a generic variable known at the cell centroid and $\mathbf{r}_i - \mathbf{r}_p$ is the position vector that connects the particle (subscript p) to the cell centroid (subscript i). The next step in the simulation is the evaluation of the Favre filtered averages fo the quantities of interest. This is achieved by considering particles within a volume centered at the point of interest. For a generic variable $Q(\phi)$:

$$\langle Q \rangle_L \approx \frac{\sum_{n\in\Delta_E} w^{(n)} \hat{Q}(\phi^{(n)})}{\sum_{n\in\Delta_E} w^{(n)}} \tag{3.4}$$

where $w^{(n)}$ is the particle weight described in Sec. 3.2.1 and Δ_E is the length scale that characterizes the "ensemble domain" in which the SFMDF is discretely represented and in which the statistical moments of interest are calculated. A finite size domain is required by the fact that, with probability one, no particles will coincide with the point [12]. There are many ways in which the ensemble domain can be constructed. In this work we chose to use a simple grid-cell kernel function

$$h_i(\mathbf{x}) = \begin{cases} 1 & \text{if } \mathbf{x} \text{ is in cell i} \\ 0 & \text{otherwise} \end{cases} \tag{3.5}$$

so that only the particles that belong to the ensemble domain are considered for the calculations of the moments. The ensemble domain is centered around the cell centroid and it can have any shape although in this work we only consider hexaedron and spherical domains. Numerically, the specification of the size of the ensemble domain is an important issue because it is a trade-off between two conflicting requirements. Ideally, it is desired that $\Delta_E \to 0$ to reduce artificial diffusion, while the number of particles inside the ensemble domain should be infinitely large to avoid statistical error. A compromise between statistical accuracy and diffusive accuracy has to be find and an optimum value for Δ_E cannot be specified *a priori* [12]. Some results of Chapter 4 show the effect on the results of varying the ensemble domain size. Fig. 3.2 shows three possible ensemble domains.

The last step in the Monte Carlo simulation of the SFMDF is to calculate the change of composition of the particles due to mixing and chemical reactions. This can be achieved by integrating Eq. 2.50

$$\frac{d\phi_\alpha^+}{dt} = -\Omega_m(\phi_\alpha^+ - \langle\phi_\alpha\rangle_L) + \hat{S}_\alpha(\phi_\alpha^+) \tag{3.6}$$

directly to simulate these two effects simultaneously. Alternatively the mixing part can be integrated analytically and the effect of chemical reactions is determined by evaluating the fine grained reaction rates $S_\alpha^{(n)} = \hat{S}_\alpha(\phi^{(n)})$ [1].

[1] Another advantage of performing the chemical reaction step last is to allow fast chemical reactions to return to their 'local equilibrium' states

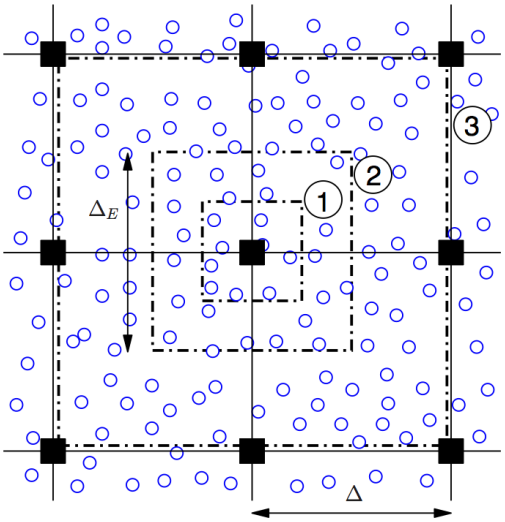

Figure 3.2. Schematic of three possible ensemble domain sizes. Squares denotes cell centroids and circles denore the MC particles. Taken from [28].

3.2.1 Particle Weighting Procedure

In this work, non-uniform weights $w^{(n)}$are assigned to each individual Monte Carlo particle to reduce the computational overhead and use the simulation particles more "efficiently". There are three main cases where particle-based weights are beneficial:

1. *Stretched grids.* Each particle can be thought to represent a fluid element of mass $w^{(n)}\Delta m$, where Δm is the unit mass which, for a constant-density flow, is defined as [18]

$$\Delta m = \frac{\rho V}{N_P} \tag{3.7}$$

where ρ is the average fluid density, V the total volume of the domain and N_P is the total number of particles used to describe the flow. If all the particles had the same weight, e.g. $(W^{(n)} = 1)$, the expected number of particles in each cell would be proportional to the cell volume. That implies that there would be less particles in smaller cells, where usually the the gradients are larger, and where a more accurate description of the flow is desirable.

2. *Variable-density flows.* When the density is not constant, it can be shown that [16],

$$\langle \rho \rangle_\ell \approx \frac{\Delta m}{\Delta V} \sum_{n \in \Delta_E} w^{(n)}, \tag{3.8}$$

where ΔV_E is the volume of ensemble domain. If no weights were used, the particle number density would decrease significantly in regions of high temperature, which is

usually where chemical reactions are taking place and a larger number of particles is needed.

3. Finally, particle-based weights allow to place particles "intelligently" , e.g. by diminishing the number of particles used in regions where is known that the degree of variability of the flow is low.

In addition of being assigned at the beginning of the computation, particle-based weights can also be modified during the course of the simulation. Several algorithms can be employed to 'clone' heavy particles and to 'cluster' light ones in order to maintain a fixed particle weight in the cell. This has the advantage to maintain a uniform statistical error throughout the domain [18].
It is useful to note that both Eq. 3.7 and 3.8 are exact in the limit of $\Delta_E \to 0$.

3.2.2 Particle tracking on 3D unstructured meshes

The hybrid coupling between the Eulerian finite volume fluid solver and the Lagrangian Monte Carlo method requires every stochastic particle to be univocally associated with a grid element at any simulation time. To this aim a robust and efficient algorithm which is able to track particles on arbitrary three-dimensional unstructured mesh is needed. For this work we chose to employ the *convex polyhedron* method proposed by Subramaniam and Haworth[26] with some small modifications. This method is well suited for a face-based data like the one used by the fluid solver. The computational domain is decomposed into arbitrary non-overlapping polyhedra, which coincides with the computational elements used by the fluid solver. In the following each variable that is associated to a computational element will be denoted with a subscript i, whereas the subscript j will be used to denote variables linked to a face. Each element has $N_f^{(i)}$ faces and a set of connectivity information that links each element to its faces. Each face carries the location of its centroid ${x_c}^j$, a normal unit vector $\widehat{n}^j$ pointing outside of the element and a connectivity pointer with the indexes of the two neighbouring elements. With reference to Fig. 3.3 particle n, which initially has position $x^{(n)}(t)$ and belongs to element i_1 has to be moved to the new location $x^{(n)}(t+\Delta t)$, which is inside element i_3. The particle moves on a straight line and its velocity is $v^{(n)} = \Delta x/\Delta t$. The first step is to build, for all the four faces of element i_1, the particle-to-face-heights $h^{(j)}$. The time it will take for the particle to intersect the jth face of i_1 is simply $t^{(j)} = h^{(j)}/(v^{(n)} \cdot \widehat{n}^j)$, where the denominator is the component of the particle velocity normal to the face. The minimum time to intersect one of the faces of i_1 is $t_{min}^{(i)} = min_{j=1}^{N_f(i_1)} \left[max\left[0,t^{(j)}\right]\right]$. If $t_{min}^{(i_1)} > \Delta t$ then the particle is still inside element i_1. If $t_{min}^{(i_1)} < \Delta t$, the particle is moved to the intersection point of the face $x_{int} = x^{(n)}(t) + v^{(n)} t_{min}^{(i_1)}$, its time step is decremented by $t_{min}^{(i_1)}$ and appropriate actions can be taken depending on the type of face it intersected. For example, if it is an internal face the particle element pointer is updated to the the new element it now belongs to. If it is a boundary face, the appropriate boundary condition (symmetry, periodicity, inflow, outflow) can be easily assigned. In the example of Fig. 3.3, the particle is first moved on $x_{int}^{(i_2)}$ and, as j_2 is an internal face, its element pointer is updated to i_2. The same procedure

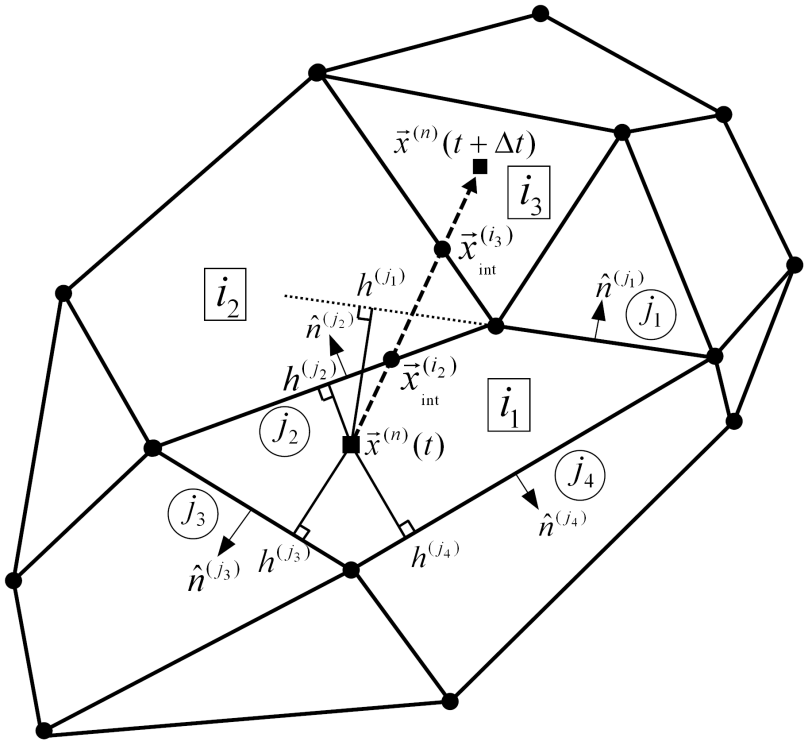

Figure 3.3. Two-dimensional example of particle tracking on unstructured meshes. Element i_1 has four faces denoted by j_1, j_2, j_3 and j_4.

is repeated for al the faces of element i_2 and the particle is moved again on $x_{int}^{(i_3)}$ and its pointer updated to on i_3. Now the remaining Δt is the less than the minimum time to reach any of on i_3 faces and thus the particle will reach its final position $x^{(n)}(t+\Delta t)$.

3.2.3 Boundary Conditions

There are four types of boundary conditions that have been implemented in the Monte Carlo solver. These are

1. Outflow
2. Wall / Symmetry
3. Inflow
4. Periodic Boundary

At an outflow boundary the mean velocity vector will point out of the flow domain. All the particles that cross an outflow face are simply eliminated.
In the case of a symmetry or a wall condition, the particle is reflected back into the domain

(Fig. 3.4).

At an inflow boundary the mean velocity vector will point into the flow domain. The

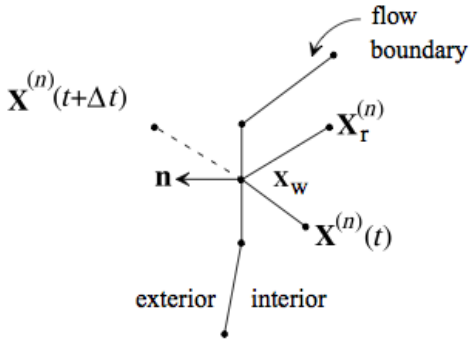

Figure 3.4. Sketch of a reflective boundary condition. Taken from [18].

total mass entering the domain during the time step Δt is

$$\Delta m_{in} = \rho_{in} S_{in} \langle U \rangle_{in} \Delta t \tag{3.9}$$

where ρ_{in} and $\langle U \rangle_{in}$ are the density and mean velocity of the incoming flow and S_{in} is the inflow surface area. A fixed number of particles per inflow cell ${N_P}^{in}$are added into the domain with weight

$$w^{(n)} = \frac{\Delta m_{in}}{{N_P}^{in} \Delta m} \tag{3.10}$$

The new particles are placed at the inflow face centroid and their composition correspond to the inflow composition. Because of the diffusion term in Eq. 3.2, a particle may attempt to leave the domain even if it is an inflow. In this case the particle is reflected back inside in the same way as in the symmetry/wall case.

In the case of a periodic boundary condition, the particles are translated to the corresponding periodic face. In a simulation where only symmetry/wall and periodic boundary conditions are present, the total number of simulation particles is conserved.

3.3 Coupling between the FV and the MC solver

One advantage of the hybrid FV/MC formulation is that the coupling between the two codes is minimal and this fact allows us to write the whole Monte Carlo routine as a complete separate module that can be activated at user's choice.

The flow chart for a typical FV/MC hybrid simulation is displayed in Fig. 3.5. The Finite Volume solver and the Monte Carlo one procede in a "serial" way. At the beginning of the simulation, both the FV variables and the MC particles are initialized. A fixed number of particles (NPC) are created for every cell and each particle is assigned a weight

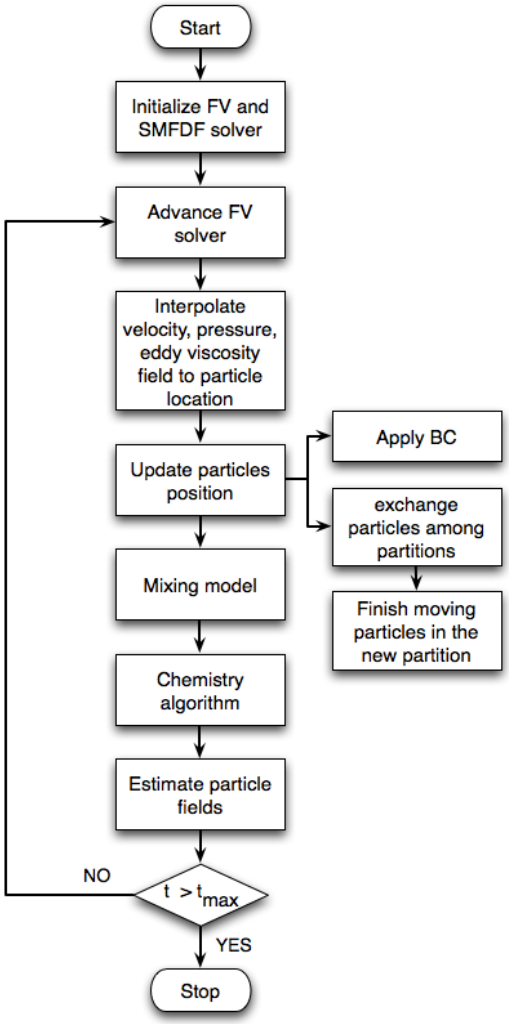

Figure 3.5. Flow chart for a hybrid FV/MC simulation.

according to the local fluid density. As the simulation proceeds, the FV solver is advanced first and cell-centered values of all the hydrodynamic variables are updated. Next the Monte Carlo module is called and the particles are moved to their new locations based on the solution of the Stochastic Differential Equations (Eq. 3.2). The updated velocity, pressure and eddy viscosity fields are interpolated to the particle location. Whenever a particle hits a boundary face, the appropriate boundary condition is applied (Sec. 3.2.3). All the particles that hit a face which is on the boundary between two partitions are flagged and exchanged at the end of the moving algorithm. It is much more computationally efficient to exchange the particles all at once "in trains" rather than one by one. As soon

as the particles are delivered to their new partition, they are moved for the remaining time-step. After the composition is updated because of mixing and chemical reactions, ensemble averages are calculated and the relevant quantities are passed back to the Finite Volume solver to use in the next iteration.
The Monte Carlo solver uses the same domain partitioning that is generated for the FV solver by the graph partitioning library Metis [25]. Fig. 3.6 shows an example of such a partitioning on a cubic domain. It must be noted that Metis generates partitions while minimazing some penalty functions like the latency of data transfers and load imbalances. Although this is very efficient for a standard Finite Volume calculation, it may not be the ideal partitioning for the Monte Carlo solver in cases with complex chemistry [28].

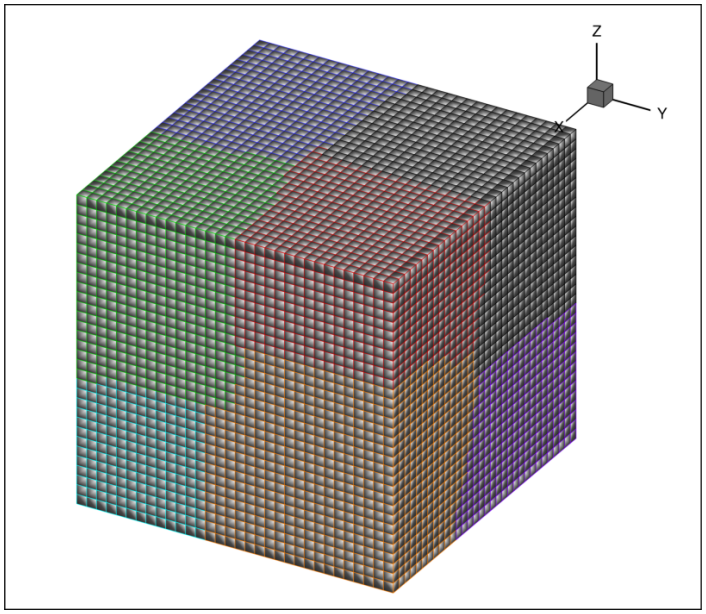

Figure 3.6. Example of domain partitioning by Metis on a 32^3 grid with 8 processors.

Chapter 4

Results

In this chapter we present the results of two and three-dimensional temporal developing mixing layer simulations and of three-dimensional turbulent wake. The main objectives of these simulations are

1. To demonstrate the consistency of the SMFDF / Monte Carlo procedure.
2. To show the dependence of the Monte Carlo solution on the numerical parameters.
3. To investigate the performance of SMFDF for compressible flows.

For the first objective, the transport equations for the first two scalar moments (Eq. 2.46 and 2.47) are solved using the conventional LES Finite-Volume solver and the results are compared with those obtained using the SFMDF/Monte Carlo procedure. The FV-MC consistency can be checked only in the case of a non-reacting flow as, for a reacting case, the chemical source term is treated in a different manner by the two methods.
The second objective is achieved by comparing the solutions obtained varying the most important numerical parameters in the Monte Carlo simulation, such as the initial number of particles per cell (NPC) and the size of the ensemble domain (Δ_E). The effect of the turbulence model, the grid size and the Reynolds number are also investigated.
The performance of the Monte Carlo procedure for compressible flows is assessed by means of three-dimensional low speed simulations where an non-uniform density is initially prescribed. Furthermore two-dimensional simulations are conducted at a high subsonic Mach number, where compressible effects become relevant and shock waves are formed.
The temporal developing mixing layer consists of two co-flowing streams travelling in opposite directions with the same speed [27], [29], [31]. The streamwise, cross-stream and, if present, spanwise directions are denoted by x and y and z, respectively. The velocity components in these directions are u, v and w.
For the three-dimensional mixing layer, we follow the setup suggested by Vreman et al. [30]. The domain is a cubic box with $0 \leq x \leq L$, $-L/2 \leq y \leq L/2$, $0 \leq z \leq L$. The length in the streamwise direction is large enough to allow for the roll-up of two large vortices and one subsequent pairing of these vortices. Periodic boundary conditions are assigned in the streamwise (x) and spanwise (z) directions, while along y a symmetry

condition is imposed. The initial velocity profile is initialized with a hyperbolic function with $\langle u \rangle_L = 1$ on the top stream and $\langle u \rangle_L = -1$ on the bottom one. The formation of turbulent structures is expedited by adding eigenfunctions-based perturbations to the flow [30]. The flow variables are normalized with respect to the half initial vorticity thickness, $L_r = [\delta_v(t=0)/2$; $\delta_v = \Delta U / |\partial \langle u \rangle / \partial y|_{max}$, where ΔU is the velocity difference across the layer. The reference velocity is $U_r = \Delta U/2$. The Reynolds number based on the reference velocity and length scale is defined as

$$Re = \frac{U_r L_r}{\nu_r}. \tag{4.1}$$

For the three-dimensional simulations, the convective Mach number, defined as

$$M_c = \frac{u_1 - u_2}{c_1 + c_2} \tag{4.2}$$

is held fixed at $M_c = 0.2$. In Eq. 4.2 the subscript 1 and 2 refers to the upper and lower stream, respectively, and c is the speed of sound.
We follow the evolution of a passive scalar A, which is also initialized with a hyperbolic tangent profile with $\langle A \rangle_L = 1$ on the upper one and $\langle A \rangle_L = 0$ on the bottom one.
For the two-dimensional simulations, we follow the case proposed by Yee [32], [33] at a convective Mach number of $M_c = 0.8$. At this Mach number there are shock waves (shocklets) that form around the vortices and the problem is to compute accurately the vortex evolution while avoiding oscillations around the shock. Fig. 4.1 shows a schematic

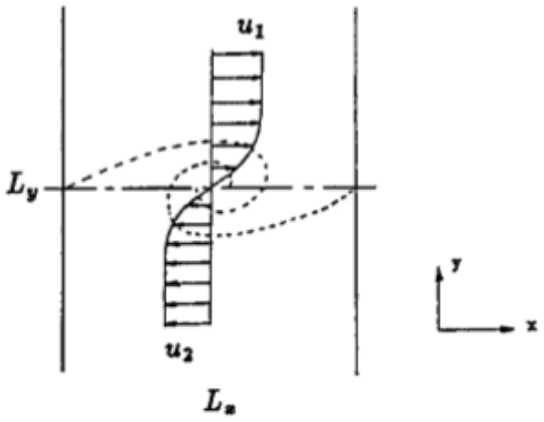

Figure 4.1. Schematic showing the vortex pairing in the two-dimensional mixing layer. This image is taken from [33].

of the physical problem. The velocity is initialized with a hyperbolic tangent profile and the temperature is determined from an assumption of constant stagnation enthalpy. The Reynolds number defined by the velocity jump, vorticity thickness, and kinematic viscosity

at the freestream temperature is set equal to 1000. Disturbances are added to the velocity components in the form of simple waves. For the normal component of velocity we have the perturbation

$$v' = \sum_{k=1}^{2} a_k \cos(2\pi k x/L_x + \phi_k) \exp(-y^2/b) \tag{4.3}$$

where $L_x = 30$ is the box length in the x-direction and $b = 10$ is the y-modulation. The u-velocity perturbations are found by assuming that the total perturbation is divergence free and $a_1 = 0.01$, $\phi_1 = -\pi/2$, $a_2 = 0.05$ and $\phi_1 = -\pi/2$. The domain is $[0,30] \times [-50,50]$ and a the grid is uniform in the x-direction, while a hyperbolic sine stretching is used in the y-direction.
In the three-dimensional planar wake simulation a slower stream is issuing through a nozzle, or slot, at a velocity $U_0 = 25$ m/s, into a co-flowing stream with velocity $U_{\text{inf}} = 100$ m/s. The wake temperature is $T_0 = 400K$, while the co-flow is at $T_{\text{inf}} = 300K$. The Reynolds number based on the velocity difference $\Delta U = U_{\text{inf}} - U_0$, the slot height D and the density and viscosity of the co-flow is $Re = \rho_0 \Delta U D/\mu_0 = 2150$, while the Mach number is $M = 0.3$. The pressure is held constant at $p_{atm} = 101125$ Pa, so that the two streams have different densities. The passive scalar A is introduced in the flow with composition $\langle A \rangle_L = 1$ in the wake and $\langle A \rangle_L = 0$ in the co-flow. The Prandtl and Lewis numbers are set to $Pr = Le = 1$.

4.1 Numerical specifications

In all simulations equally-spaced hexaedra elements are employed ($\Delta x = \Delta y = \Delta z = \Delta$). For the mixing layer simulations, 32x32x32 and 64x64x64 grids are used for the three-dimensional case and 200x200x1 grids for the two-dimensional case, while a 288x176x72 resolution is employed for the planar wake. To investigate the effect of the Reynolds number on the results, the mixing layer simulations are performed at Re = 10, 25, 50, 100 and 200 for the three-dimensional case, while it is held constant at Re = 1000 and Re = 2150 for the 2D mixing layer and the wake, respectively.
The LES filter function is a top-hat with a characteristic filter length Δ_G

$$G(\mathbf{x'} - \mathbf{x}) = \prod_{i=1}^{3} \hat{G}(x_i' - x_i) \tag{4.4}$$

$$\hat{G}(x_i' - x_i) = \begin{cases} \frac{1}{\Delta_G} & \text{if } |x_i' - x_i| \leq \frac{\Delta_G}{2} \\ 0 & \text{if } |x_i' - x_i| > \frac{\Delta_G}{2} \end{cases} \tag{4.5}$$

where the filter width is taken as the cubic root of the volume of the cell, $\Delta_G = \sqrt[3]{V_i}$, and the secondary filter for the MKEV turbulent model (Δ') is taken so that $\Delta'/\Delta_L = 5$. No attempt is made to investigate the sensitivity of the results on the choice of the filter function or filter width [34].
The Monte Carlo solver is initialized by uniformly distributing a fixed number of particles in every cell throughout the computational region. The initial position of the particle inside the cell is random and the particle weight is imposed so that it satisfies the local cell

density, according to Eq. 3.8. The sensitivity of the stochastic simulation is assessed by prescribing different initial number of particles per cell (NPC) and by considering different sizes and shape for the ensemble domain (Sec. 3.2.1). For this work we used NPC = 60, 120, 240, 320 and 480. The ensemble domain is either a cubic box or a sphere and the characteristic length is the same as the cell size ($\Delta_E = \Delta$) or half of it ($\Delta_E = 1/2\Delta$).
In the case of the 3D planar wake, 60 particles per cell where initially used, for a total of about 219 million particles. The mixing model constant is held fixed at $C_\Omega = 4$ which has shown to give satisfying results for the mixing layer [16]. The MKEV turbulence model constant is $C_k = 0.020$, while no parameters are necessary for the SA turbulent model. The turbulent Schmidt and the turbulent Prandtl numbers are held fixed at $Sc_T = Pr_T = 0.7$. The three-dimensional mixing layer is simulated until $t = 80$ with a timestep of $\Delta t = 0.04$, while the two-dimensional until $t = 160$. For the 3D planar wake the timestep is $\Delta t = 0.005$, for a total simulation time of $t = 80$. A third-order explicit Runge-Kutta method is used to integrate in time.

4.2 Consistency of the SFMDF-MC method

The consistency of the Monte Carlo procedure is demonstrated by comparing the results obtained for the first two moments (hereafter denoted SFMDF-MC) with those obtained by solving the transport equations (Eq. 2.46 and 2.47) for the same moments with a conventional Finite Volume technique (denoted FV). The results are analysed both instantaneously and statistically. For the former snap-shots or scatter plots of the relevant variables are shown, while, for the latter, Reynolds averaged statistics are considered. Reynolds averaged results, denoted by an overbar, are constructed by averaging over the statistically homogeneous directions (streamwise and spanwise). All the results presented in this section are for the low Mach number three-dimensional mixing layer on a 32^3 equally spaced grid with $Re = 50$, NPC = 120 and a cubic ensemble domain with $\Delta_E = \Delta$, unless noted. Also all the figures from 4.2 to 4.11 are obtained without using a turbulence model ($\nu_T = 0$).
Fig. 4.2 show the 3D scalar field obtained from the FV and SFMDF-MC simulations. These figures, together with the iso-surface vorticity magnitude plot of Fig. 4.3, show the high degree of mixing and three dimensional structures present in the flow, which makes it a good test case to assess the performance of the SFMDF methodology.
The instantaneous contour plots of the filtered scalar mass fraction of Fig. 4.4 provide a visual demonstration of the consistency of the SFMDF-MC procedure, as the results are in close agreement with those obtained from the FV method. The scatter plots of Fig. 4.5 also corroborates the similarity of the solutions for the first statistical moment. In this chart the mass fraction computed at each point by both methods are plotted against each other for $t = 60$ and $t = 80$. The correlation coefficient for both snapshots is greater than 0.998. The Reynolds averaged results for first moment of the filtered scalar (Fig. 4.6 and 4.7) also confirm the good agreement seen in the instantaneous ones.
Another quantity of interest is the resolved (or LES) variance, defined as

$$R(a,b) = \left(\langle a\rangle - \overline{\langle a\rangle}\right)\left(\langle b\rangle - \overline{\langle b\rangle}\right)$$

Fig. 4.8 and 4.9 show the Reynolds average results of this quantity. Although still fairly good, it is clear that the agreement is somewhat slightly less good for this quantity.
The discrepancy is miuch more apparent for the second moment, the SGS variance, which is defined as $\sigma_A^2 = \langle A^2 \rangle_L - \langle A \rangle^2$. Fig. 4.10 and 4.11 show that the difference between the SFMDF and the FV solutions are over 300%. The reasons for these discrepancies lie in the fact that higher moments are more sensitive to statistical and diffusion errors than lower ones and it motivates the numerical study that is presented in the next section.

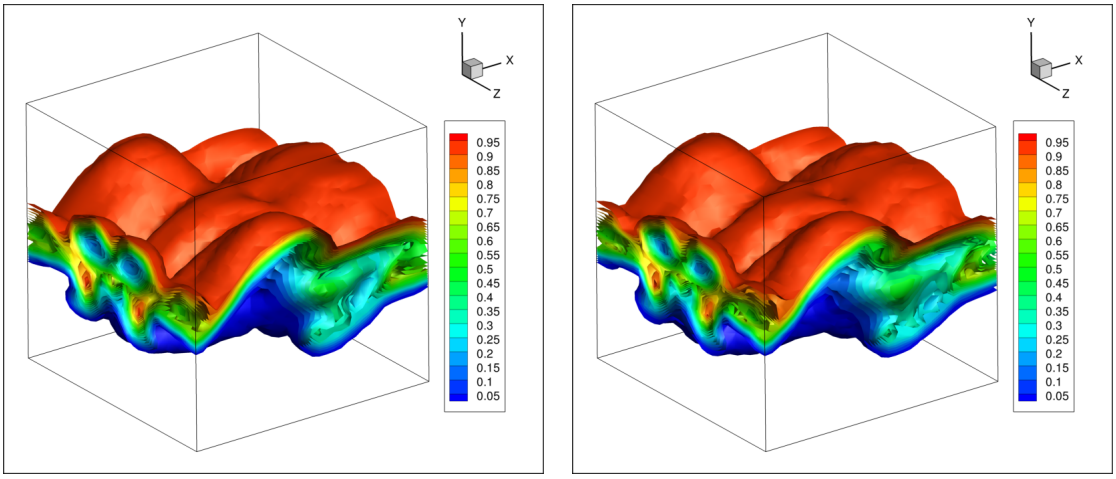

(a) (b)

Figure 4.2. Three-dimensional contour plots of the instantaneous mass fraction of the conserved scalar obtained by SFMDF (a) and Finite Volume (b).

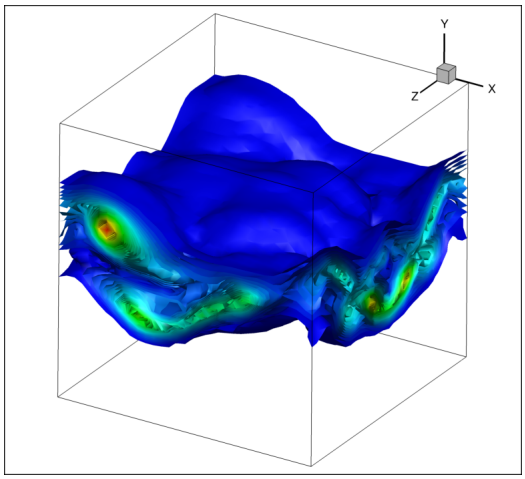

Figure 4.3. Iso-surface of the vorticity magnitude.

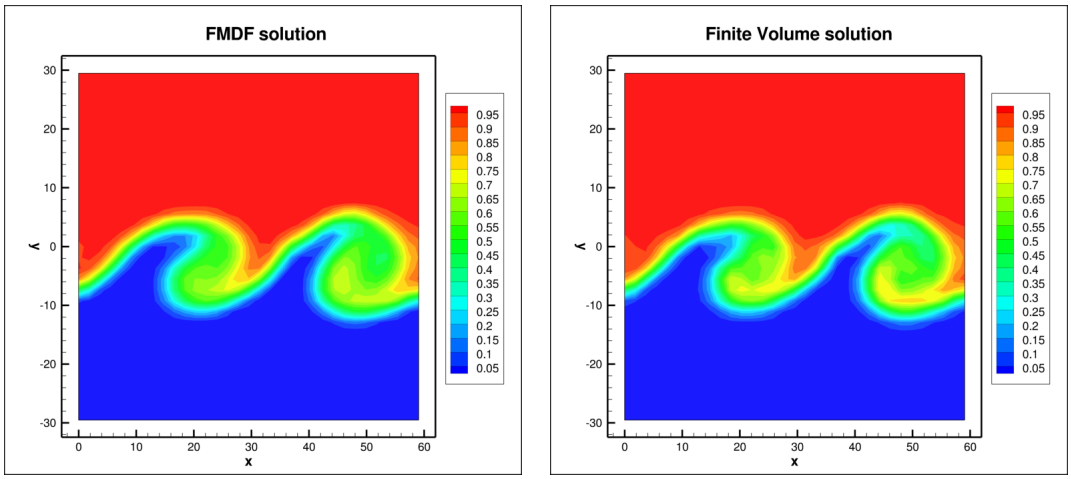

(a) (b)

Figure 4.4. Instantaneous filtered mass fraction of the conserved scalar at a slice at z=44 and t=60. (a) SFMDF, (b) Finite Volume.

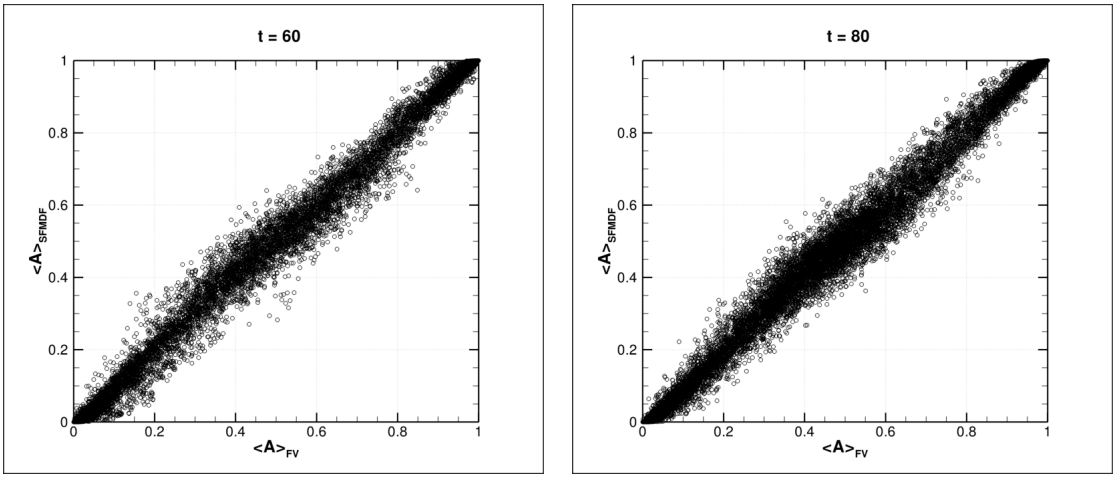

(a) (b)

Figure 4.5. Scatter plots of the filtered mass fraction of the conserved scalar calculated by SFMDF and FV at t=60 (a) and t=80 (b).

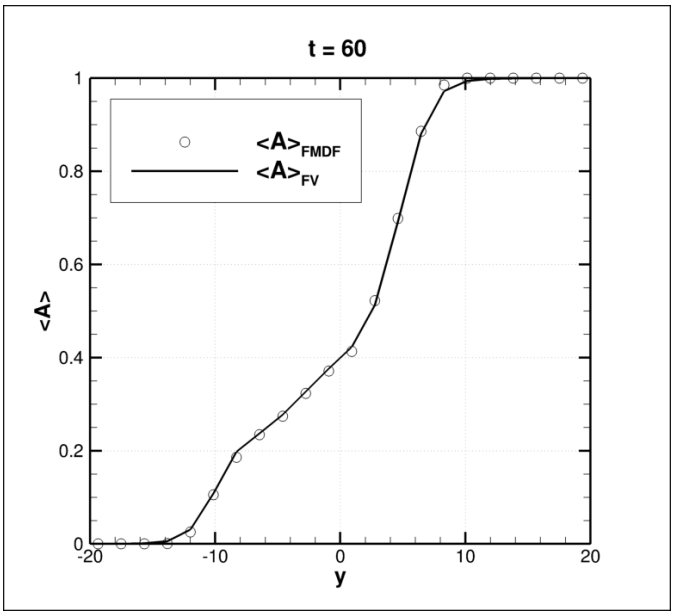

Figure 4.6. Cross-stream variation of the Reynolds averaged scalar mass fraction at t=60.

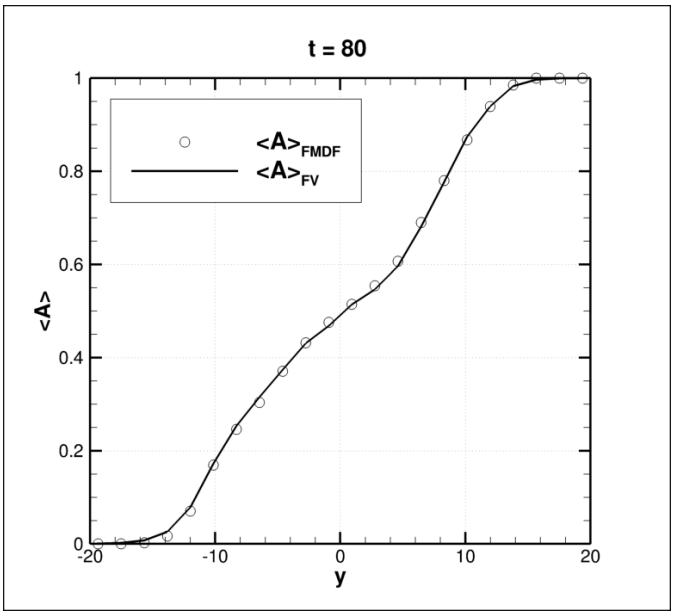

Figure 4.7. Cross-stream variation of the Reynolds averaged scalar mass fraction at t=80.

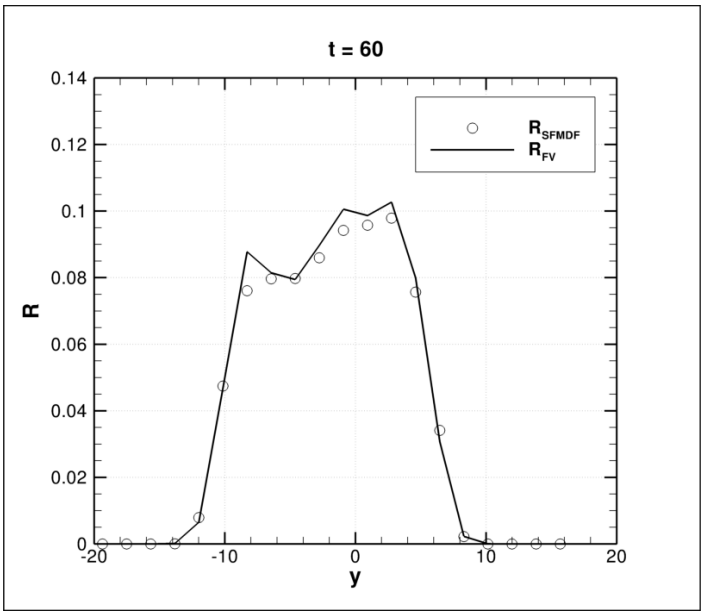

Figure 4.8. Cross-stream variation of the Reynolds averaged resolved variance $\overline{R}$ at t=60.

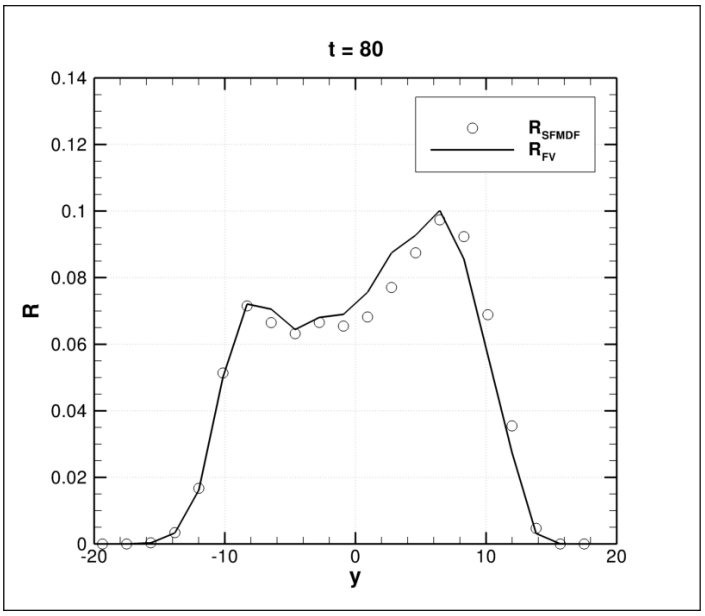

Figure 4.9. Cross-stream variation of the Reynolds averaged resolved variance $\overline{R}$ at t=80.

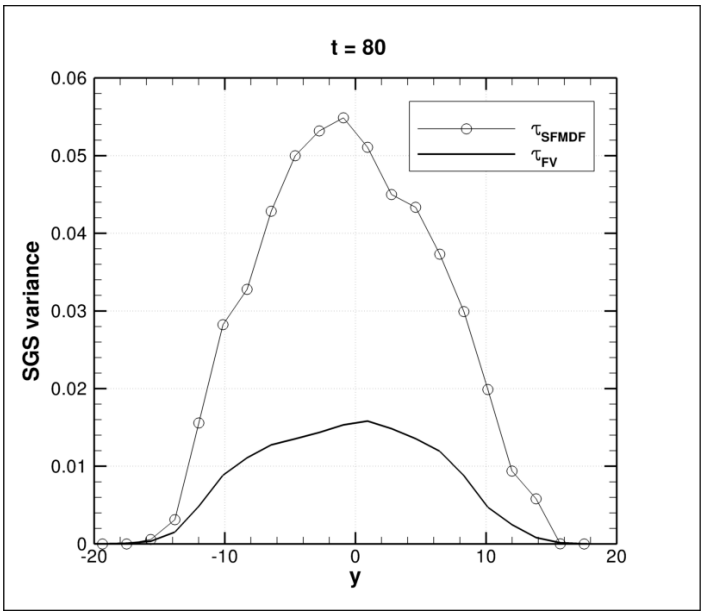

Figure 4.10. Cross-stream variation of the Reynolds averaged SGS variance $\overline{\tau}$ at t=60.

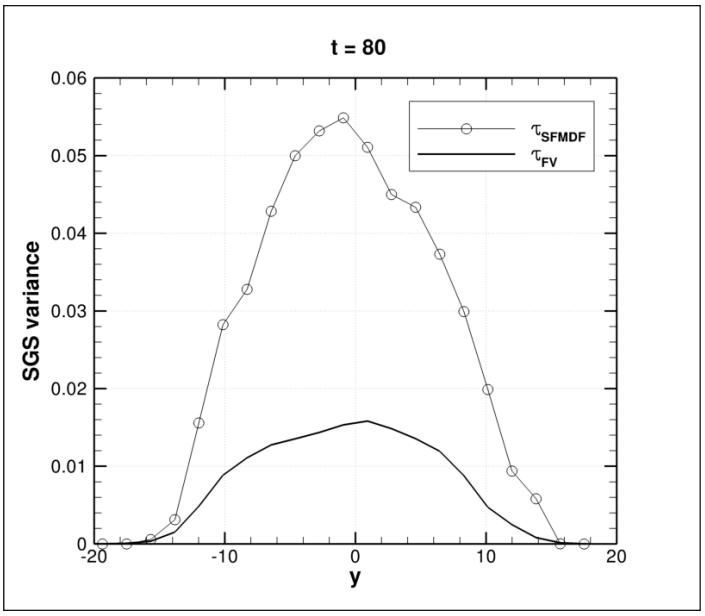

Figure 4.11. Cross-stream variation of the Reynolds averaged SGS variance $\overline{\tau}$ at t=80.

4.3 Sensitivity of the SFMDF solution on numerical parameters

In the previous section, some results for the temporal mixing layer at $Re = 50$ on a 32^3 grid without turbulence model were presented. Although the agreement between the SFMDF and FV solutions on the first moment (scalar filtered average) is very good, the variance comparison was not quite satisfactory, especially the SGS one.
The objective of this section is to investigate the sensitivity of the SFMDF results, particularly focusing on the resolved and the SGS variance, on different numerical parameters. Some of the parameters examined include

1. Grid size.
2. Reynolds number.
3. Turbulence model.
4. Initial number of particles per cell (NPC).
5. Size of the ensemble domain (Δ_E).

The first step is to assess the effect of grid resolution. Fig. 4.12 and 4.13 show Reynolds averaged results for the mean scalar mass fraction and SGS variance for two different grid sizes, respectively. While the scalar mean changes very little, grid resolution has a far greater impact on the higher moments. As the grid is refined and the sub grid scale content is reduced, both the SFMDF-MC and the FV results start to converge.
Another way to investigate the effect of the SGS influence on the solution is to hold the grid resolution fixed and vary the Reynolds number. As the Reynolds number is increased (Fig. 4.14 and 4.15), the absolute value of the SGS variance also increases, as expected, but so does the difference between the SFMDF-MC and the FV solutions. As Fig. 4.14 shows, at low Reynolds numbers the two curves lie very close but, as we reach $Re = 50$ and $Re = 100$, the relative difference between the two solutions jumps over 300% and 400%, respectively. One possible explanation may lie in the fact that, as the Reynolds is increased, so is the sub grid scale content that is being filtered and that needs to be modeled. We first tried to use the Spalart-Allmaras (SA) turbulence model but the results were not affected significantly. Following Colucci [14], we implemented in the code the Modified Kinetic Energy Viscosity (MKEV) turbulent model (Sec. 2.2.1). Fig. 4.16 and 4.17 shows the effect of adding the MKEV model on the SGS variance results on the 32^3 grid, and 64^3, respectively. The difference between the SFMDF-MC and the FV curves is significantly reduced and, most importantly, does not grow as Re is increased. Further studies might be required to assess the role of the MKEV constant (C_k) on these results.
The last two set of numerical parameters that can have an impact on the solution (initial number of particles per cell and ensemble domain size) are characteristic of the Monte Carlo solver only. The initial number of particles per cell does not seem to have a major impact on the SFMDF solution, as Fig. 4.18 and 4.19 demonstrate. This is in contrast with the size of the ensemble domain size, which does have a significant effect on the

solution. As expected, a smaller Δ_E corresponds to a more accurate SFMDF solution, as it is demonstrated by the resoved variance in Fig. 4.20 and 4.21. A similar effect is seen on the SGS variance, for both the 32^3 grid (Fig. 4.22) and the 64^3 one (Fig. 4.23). It must be noted, however, that whenever the ensemble domain is shrunk, the number of initial particles per cell must be increased so that there are enough particles inside Δ_E to compute meaningful statistics. The computational requirement of the simulation thus is increased. The impact of the NPC and Δ_E on the SFMDF solution we found here are in accordance to earlier results by various research groups [16] [14] [13]. Effectively Fig. 4.20 and Fig. 4.23 demonstrates the consistency of the SFMDF-MC results with the FV ones also for the resolved and SGS variance.

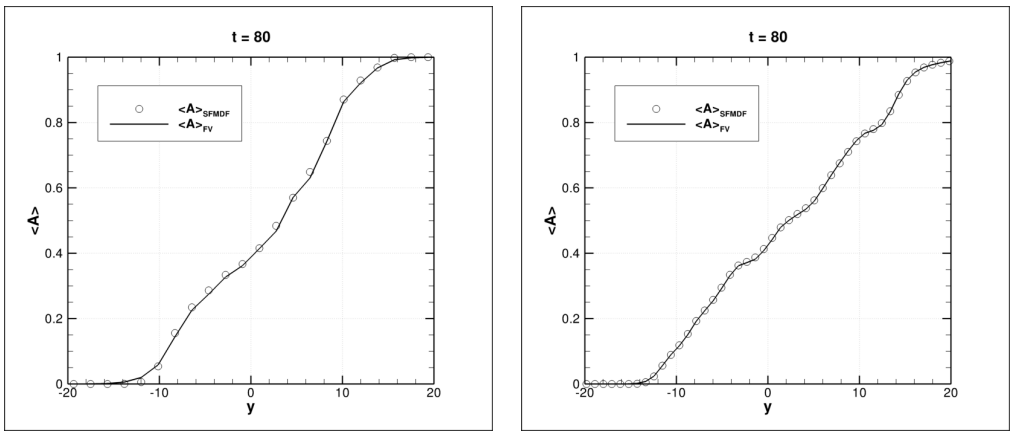

(a) (b)

Figure 4.12. Reynolds averaged scalar mass fraction. (a) 32^3 grid. (b) 64^3 grid.

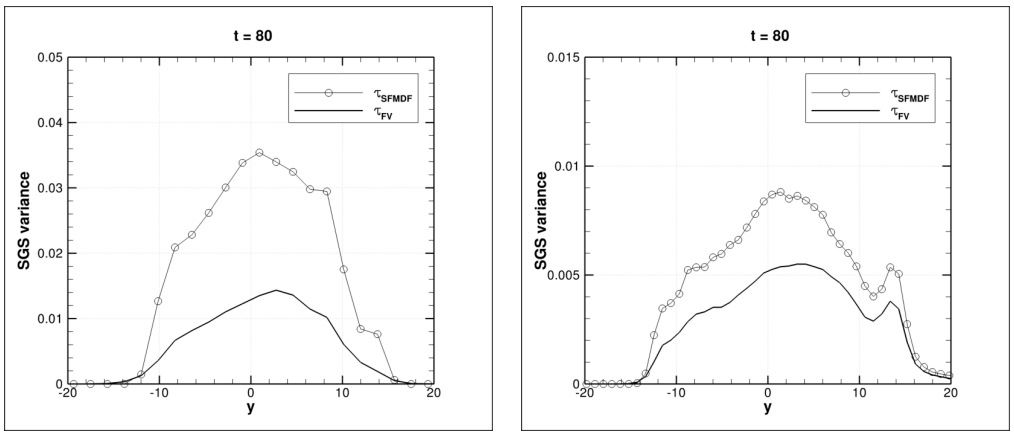

(a) (b)

Figure 4.13. Reynolds averaged SGS variance. (a) 32^3 grid. (b) 64^3 grid.

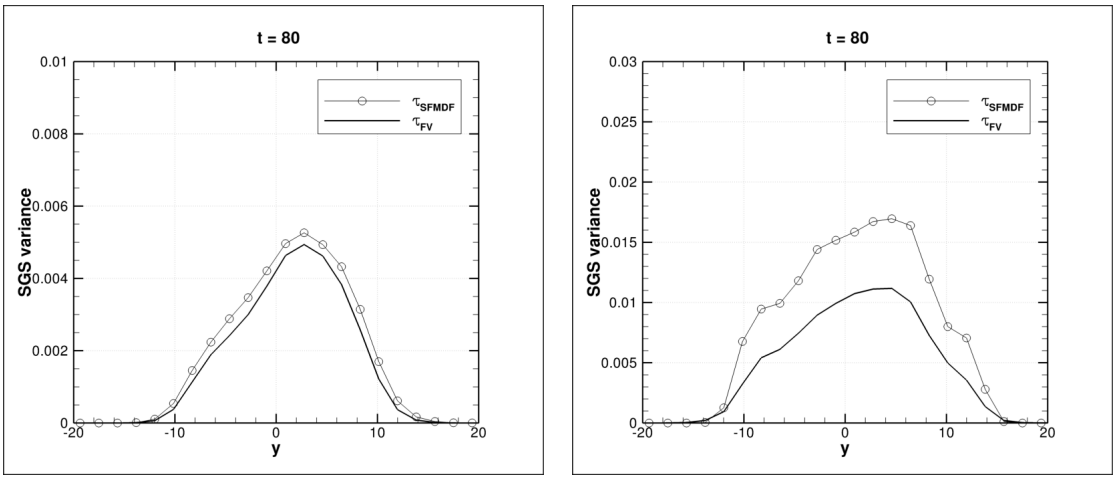

(a) (b)

Figure 4.14. Cross-stream variation of the Reynolds averaged SGS variance $\overline{\tau}$ at t=80. (a) $Re = 10$, (b) $Re = 25$

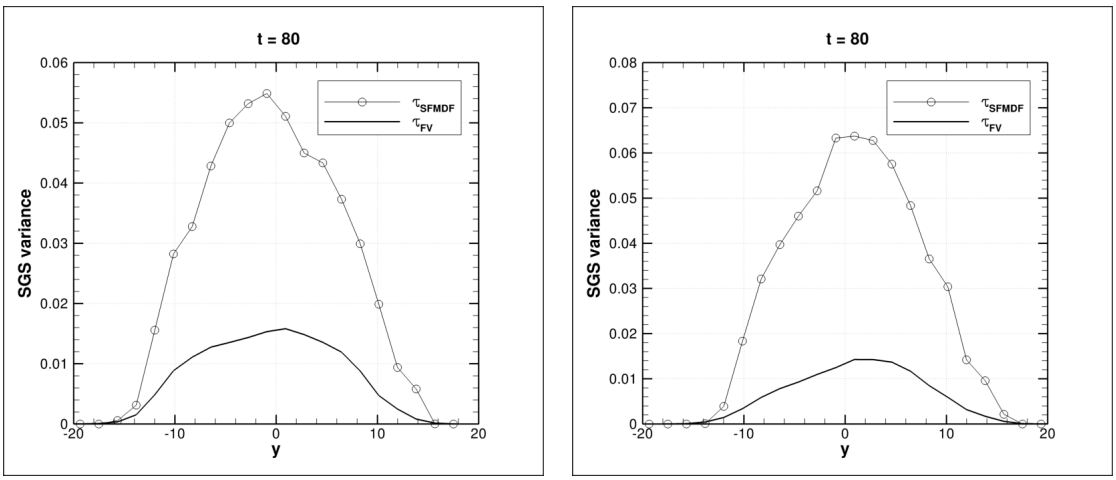

(a) (b)

Figure 4.15. Cross-stream variation of the Reynolds averaged SGS variance $\overline{\tau}$ at t=80. (a) $Re = 50$, (b) $Re = 100$

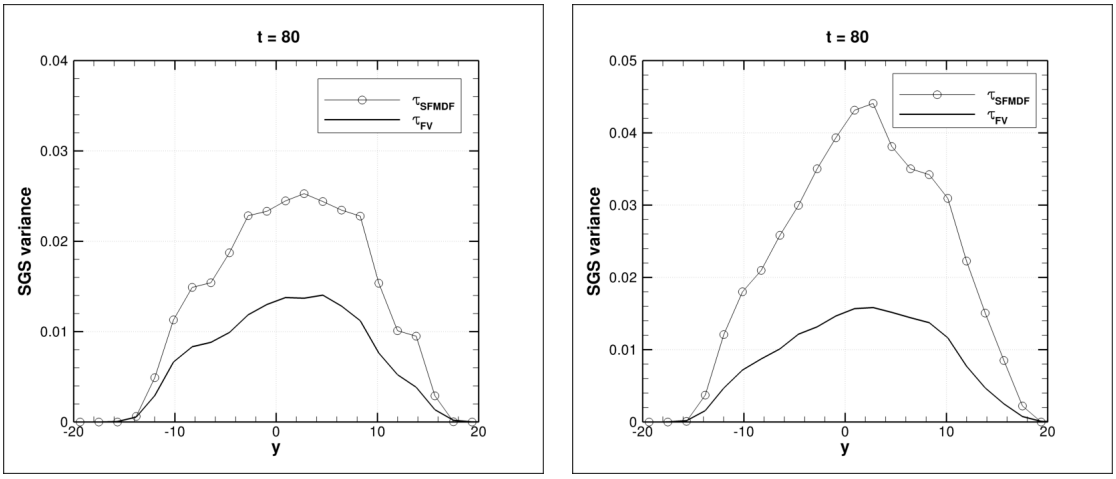

(a) (b)

Figure 4.16. Cross-stream variation of the Reynolds averaged SGS variance $\overline{\tau}$ at t=80 using the MKEV turbulence model on a 32^3 grid. (a) $Re = 50$, (b) $Re = 100$

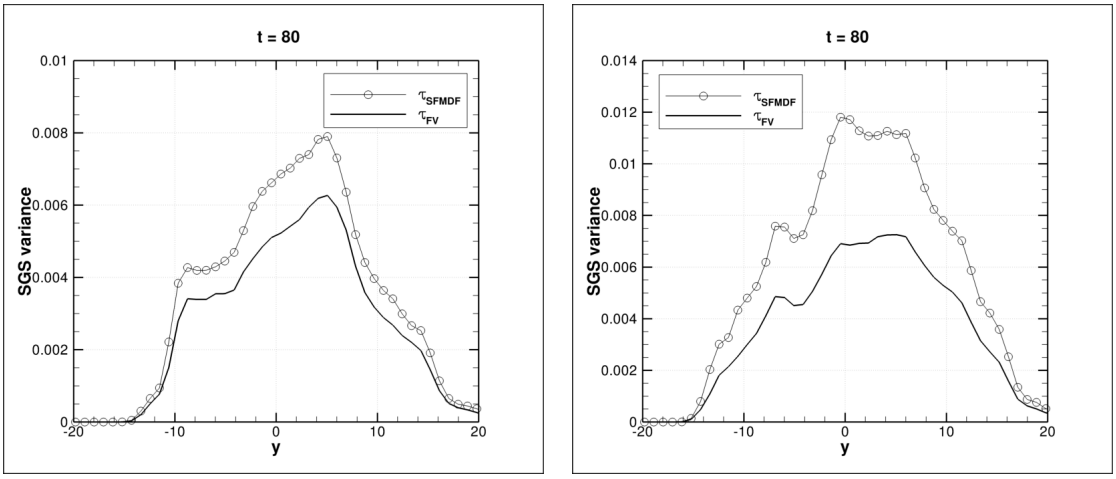

(a) (b)

Figure 4.17. Cross-stream variation of the Reynolds averaged SGS variance $\overline{\tau}$ at t=80 using the MKEV turbulence model on a 64^3 grid. (a) $Re = 50$, (b) $Re = 100$

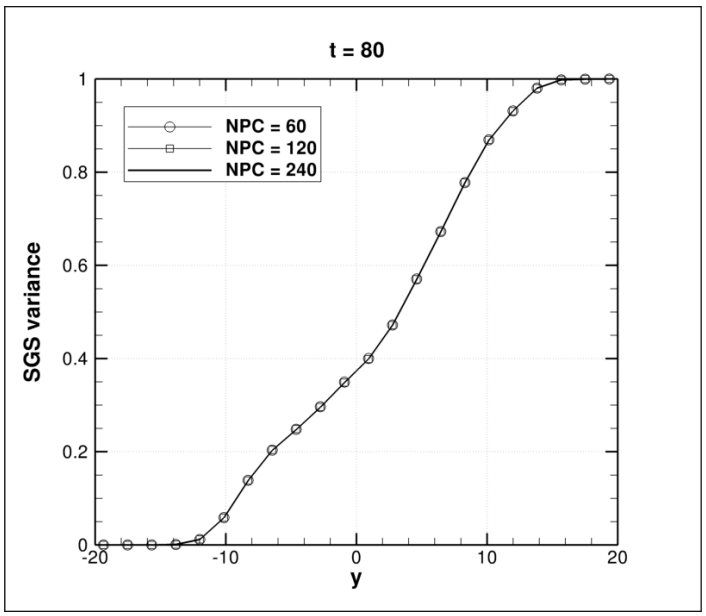

Figure 4.18. Effect of the initial number of particles (NPC) on the the Reynolds averaged scalar mass fraction at t=80.

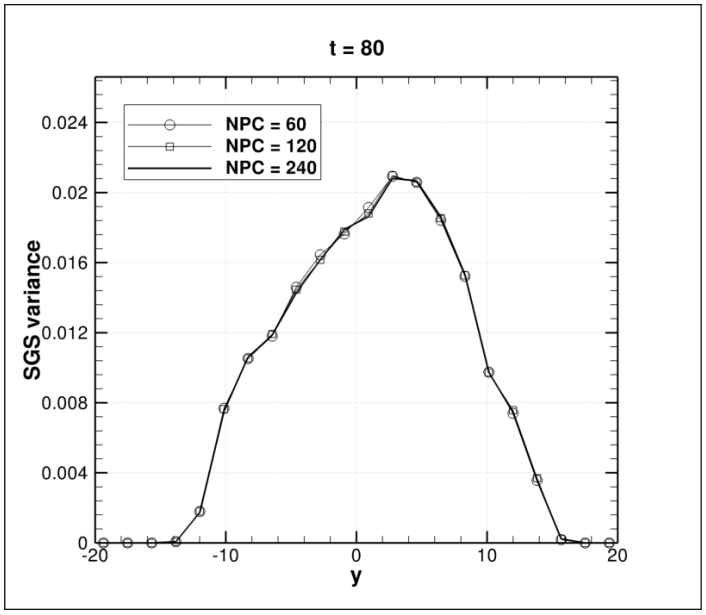

Figure 4.19. Effect of the initial number of particles (NPC) on the the Reynolds averaged SGS variance at t=80.

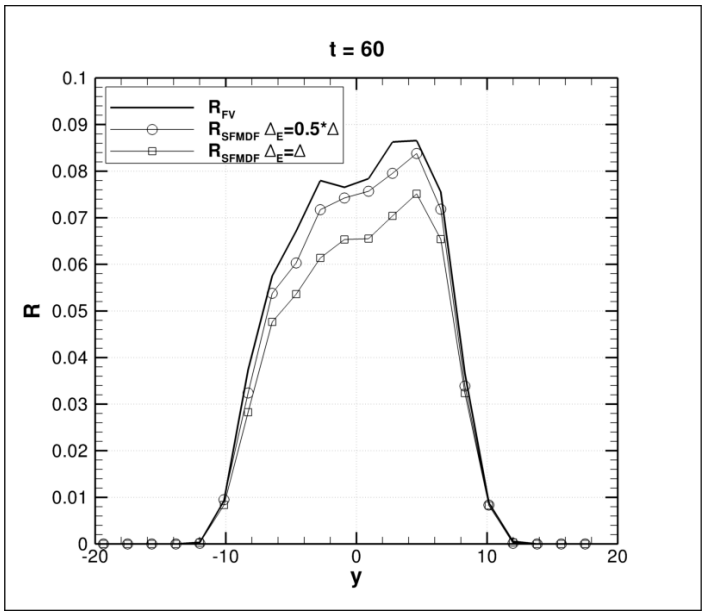

Figure 4.20. Effect of the ensemble domain size on the the Reynolds averaged resolved variance at t=60.

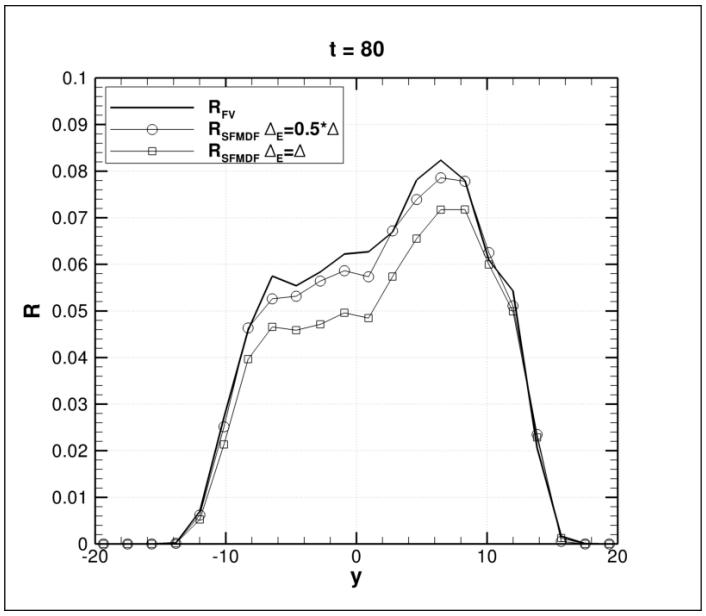

Figure 4.21. Effect of the ensemble domain size on the the Reynolds averaged resolved variance at t=80.

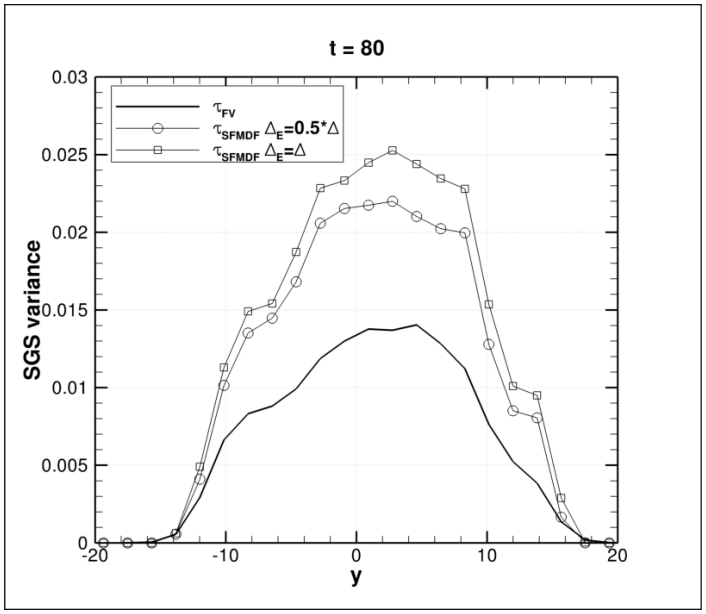

Figure 4.22. Effect of the ensemble domain size on the the Reynolds averaged SGS variance at t=80 on the 32^3 grid.

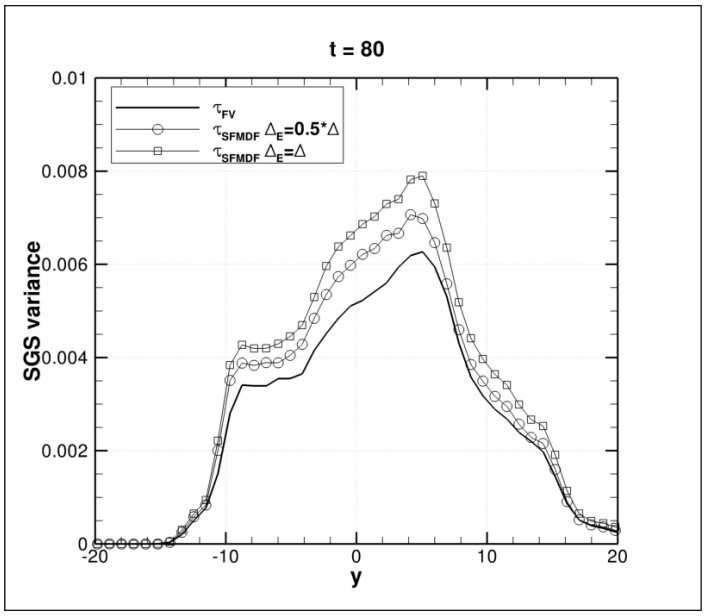

Figure 4.23. Cross-stream variation of the Reynolds averaged SGS variance $\overline{\tau}$ at t=60.

4.4 SFMDF for Variable-Density Flows

In this section we analyse the performance of the SFMDF-MC method on variable-density flows. This is achieved (i) by studying low speed flows with initial non-uniform density, and (ii) by considering a high subsonic Mach number flow, where the effect of compressibility are important.
For (i) the same three-dimensional mixing layer simulation described in the previous sections is employed. The major difference is that now the two streams are initialized with different densities. In particular, most of the simulations are carried out with the density ratio between the upper stream and the lower one, $S = \rho_1/\rho_2$, kept fixed at $S = 2$. The temperature is calculated using the perfect gas law with constant pressure. In addition to the mixing layer, results are also presented for the variable-density, 3D planar wake.
Fig. 4.24 and 4.25 show the scatter plots of the temperature for a simulation on a 32^3 grid with $Re = 50$ and using the MKEV turbulence model. The agreement between the temperature calculated from the Finite Volume and the SFMDF-MC solver is good and it is confirmed by the Reynolds averaged results which are depicted in Fig. 4.26 and 4.27.
In the SFMDF-MC methodology the density can be calculated in two different ways

1. *Using particle weights.* The sum of the weights of the particles belonging in an ensemble domain is directly linked to the local density through Eq. 3.8:

$$\langle \rho \rangle_\ell \approx \frac{\Delta m}{\Delta V} \sum_{n \in \Delta_E} w^{(n)}. \tag{4.6}$$

   This is referred to as the particle density and it is affected by statistical noise.

2. *Using the enthalpy equation and the equation of state.*

$$\langle \rho \rangle_\ell \approx \left(\frac{\sum_{n \in \Delta_E} w^{(n)} (RT^{(n)} / \langle p \rangle_\ell}{\sum_{n \in \Delta_E} w^{(n)}} \right)^{-1} \tag{4.7}$$

   This is referred to as the SFMDF density

Fig. 4.28 and 4.29 show the comparison of the Reynolds averaged results for the FV density, the SFMDF density and the particle density. As anticipated the latter show statistical noise even in these averaged results, but the overall comparison is pretty good.
To investigate (ii) the two-dimensional temporal mixing layer simulation described at the beginning of the chapter is carried out at a convective Mach number of $M_c = 0.8$. At this speed part of the flow becomes supersonic and shock waves are formed around the primary vortices, as the filtered temperature instantaneous plots clearly show (Fig. 4.30). These results are in very good agreement to the reference solution used by Yee [32]. This type of flowfield represents a good case to test the performance of the Monte Carlo scheme in the presence of discontinuities. As shown in Fig. 4.31 the instantaneous particle density field is able to represent the same discontinuities seen in the Finite-Volume density results. Also for the SGS variance, the most sensitive of the quantities for which consistency can be checked, the results are encouraging as the contour plots of Fig. 4.32 and 4.33 demonstrate.

Although the variance calculated with the SFMDF-MC method is more noisy, both the shape and the value of the two simulations compare fairly well. This is further proved by the Reynolds averaged plots of Fig. 4.34 and 4.35, where it is also shown the effect of using a smaller ensemble domain.

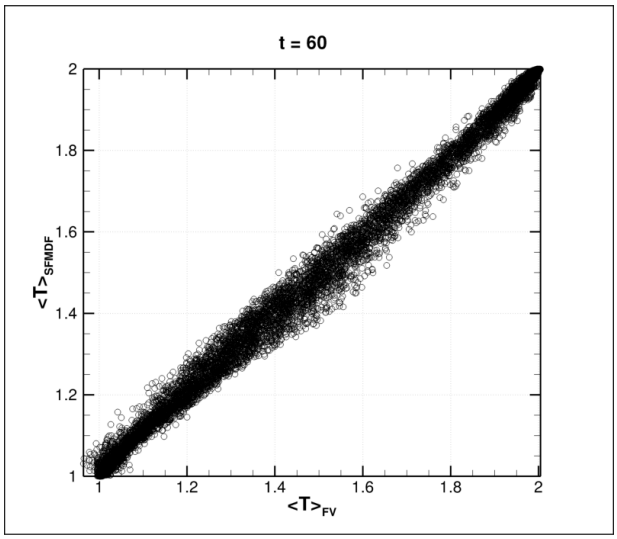

Figure 4.24. Scatter plots of the filtered temperature calculated by SFMDF and FV at t=60

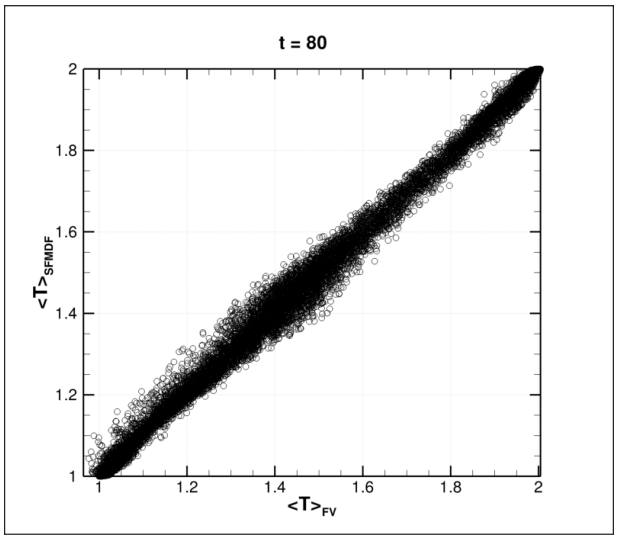

Figure 4.25. Scatter plots of the filtered temperature calculated by SFMDF and FV at t=80

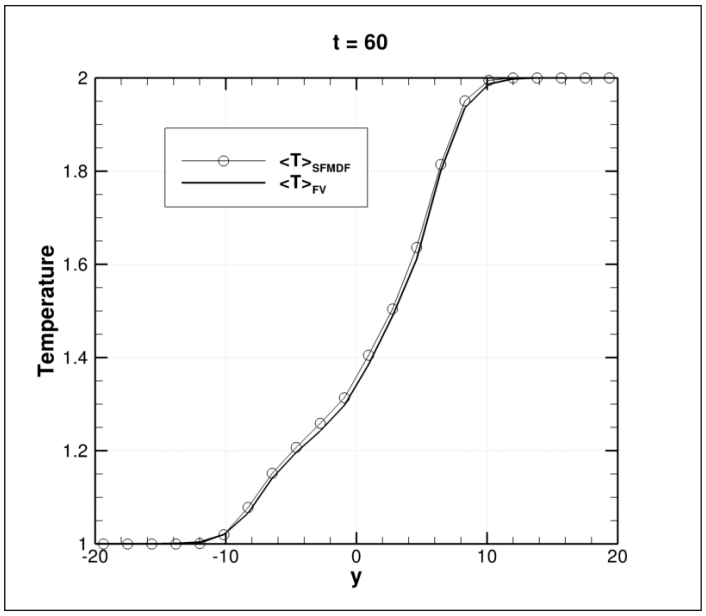

Figure 4.26. Cross-stream variation of the Reynolds averaged temperature at t=60.

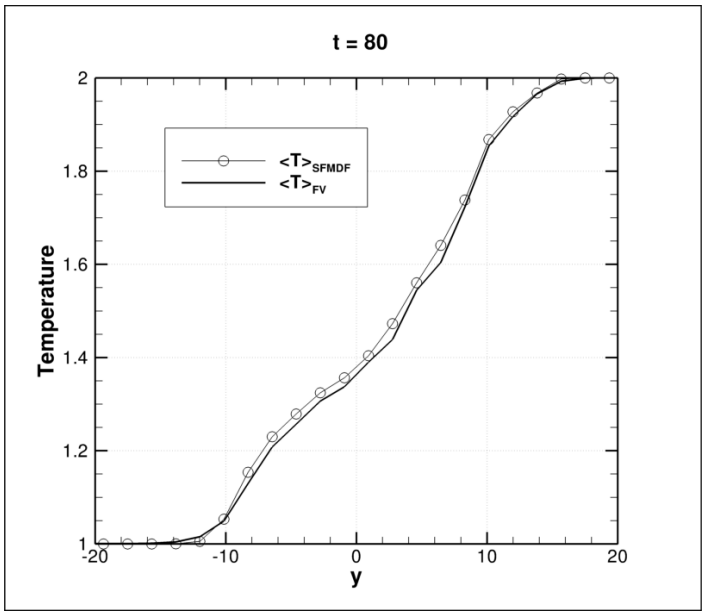

Figure 4.27. Cross-stream variation of the Reynolds averaged temperature at t=80.

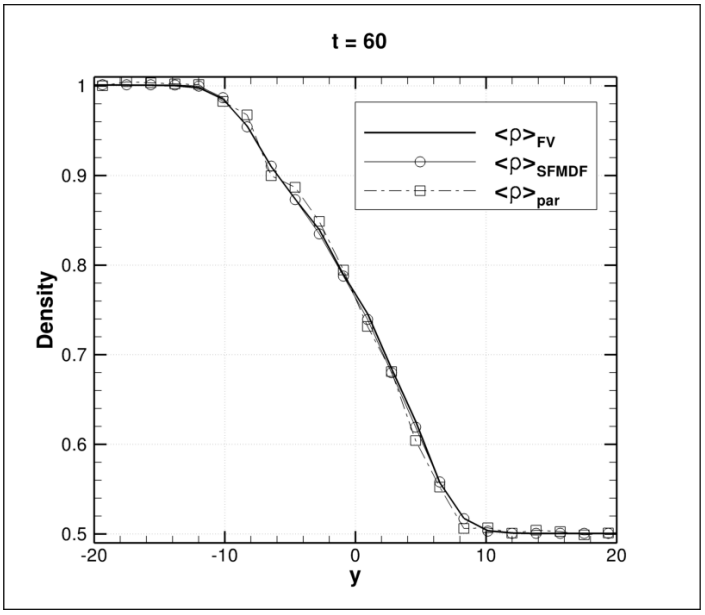

Figure 4.28. Cross-stream variation of the Reynolds averaged density obtained at t=60. Solid line Finite Volume results. Circles: Eq. 4.7. Squares: Eq. 4.6.

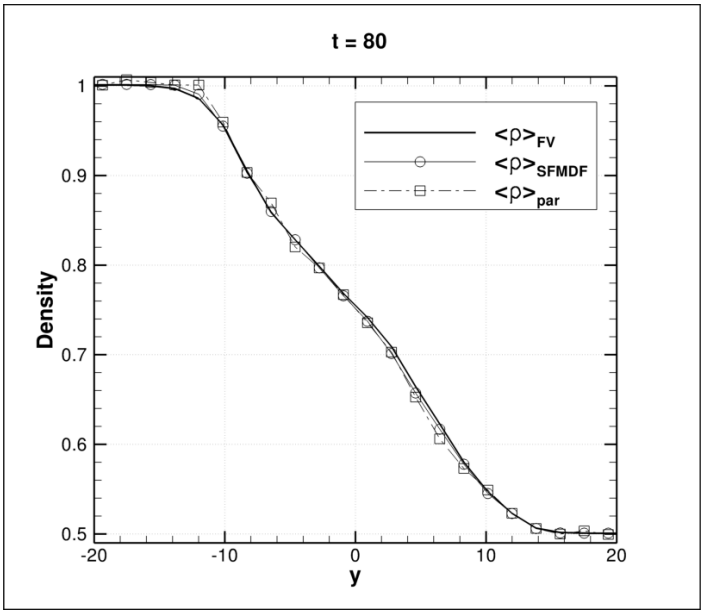

Figure 4.29. Cross-stream variation of the Reynolds averaged density obtained at t=80. Solid line: Finite Volume results. Circles: Eq. 4.7. Squares: Eq. 4.6.

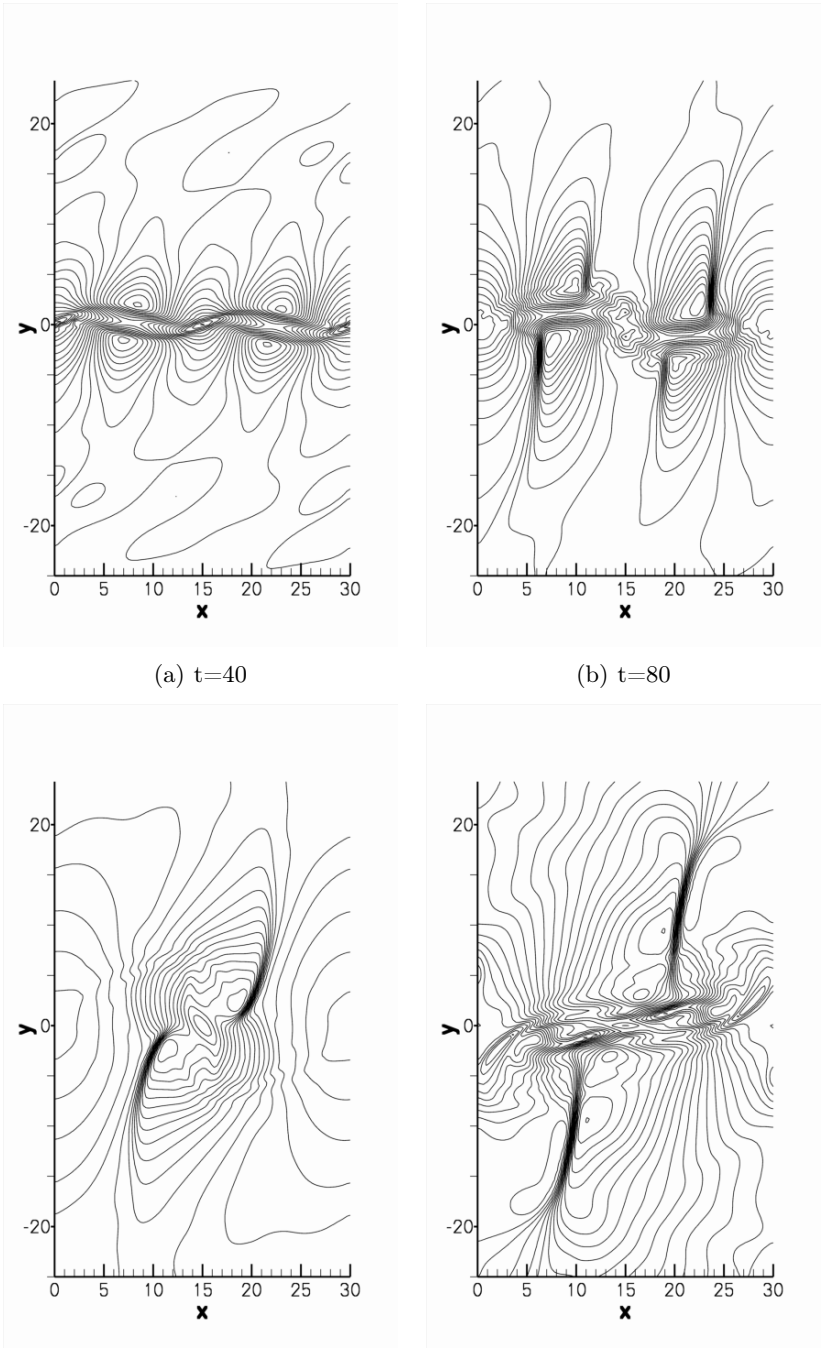

(a) t=40

(b) t=80

(c) t=120

(d) t=160

Figure 4.30. Contour plots of normalized temperature at four different stages in the vortex pairing.

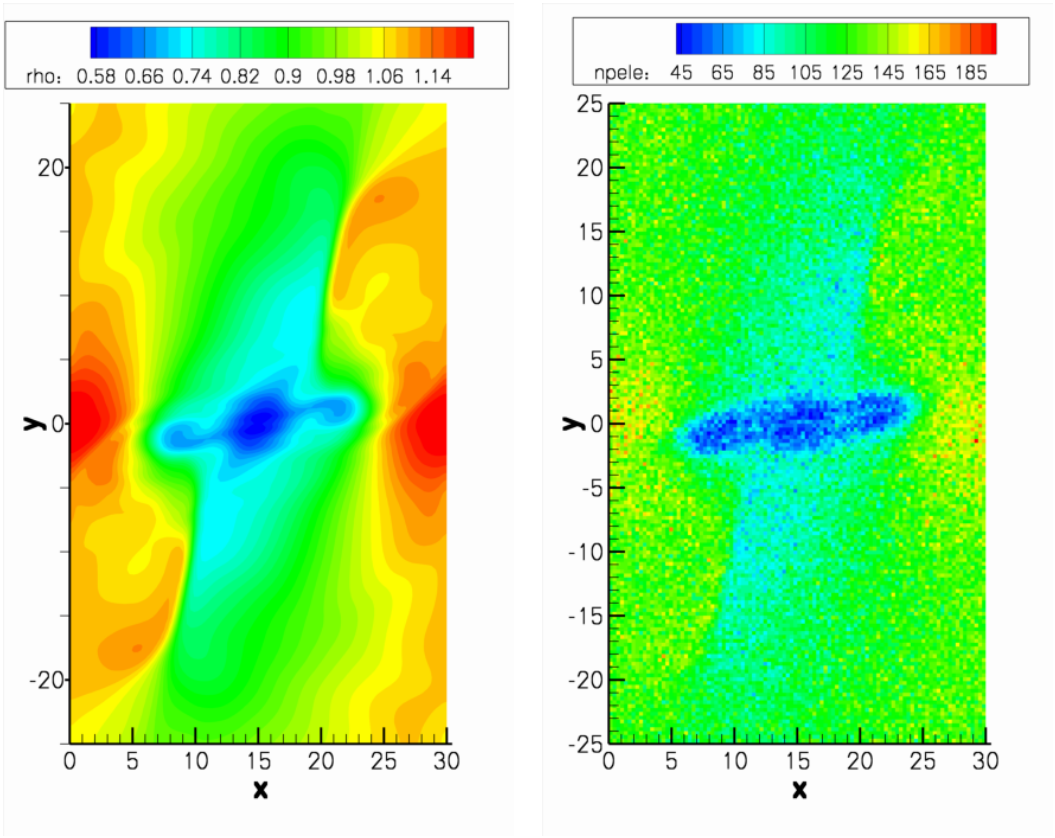

(a) (b)

Figure 4.31. Instantaneous contour plots at $t = 160$ of the filtered density (a) and the particle density Eq. 4.7 (b).

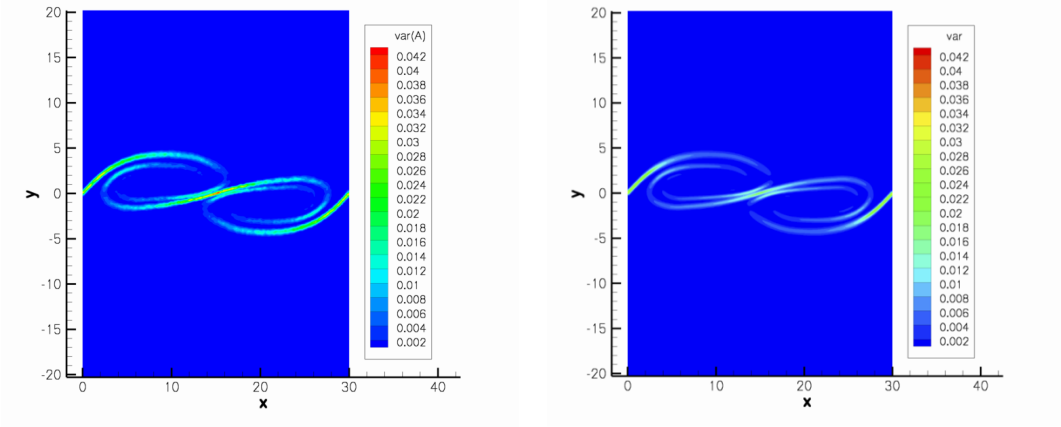

(a) (b)

Figure 4.32. Instantaneous contour plot of SGS variance at $t = 80$ for the high-speed mixing layer. SFMDF results (a). FV results (b).

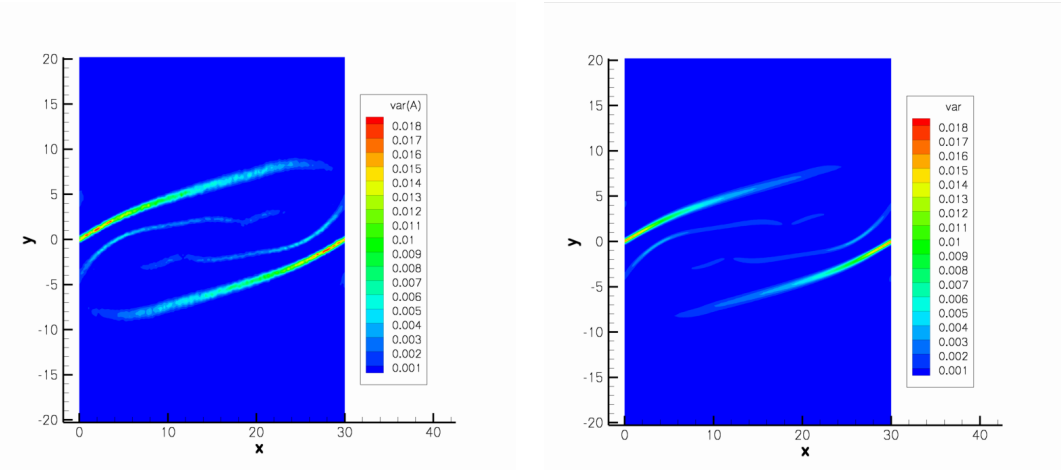

(a) (b)

Figure 4.33. Instantaneous contour plot of SGS variance at $t = 160$ for the high-speed mixing layer. SFMDF results (a). FV results (b).

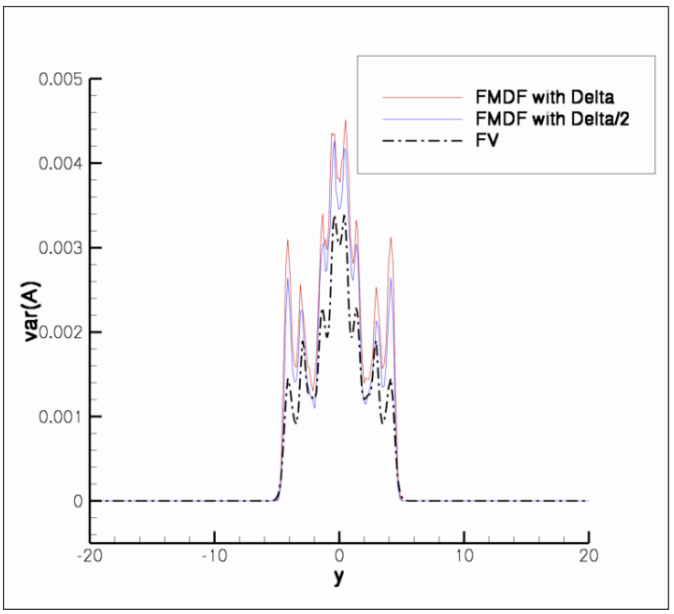

Figure 4.34. Cross-stream variation of the Reynolds averaged SGS variance for the compressible mixing layer at $t = 80$. Red line SFMDF with $\Delta_E = \Delta$, blue line SFMDF with $\Delta_E = 1/2\Delta$, black line FV.

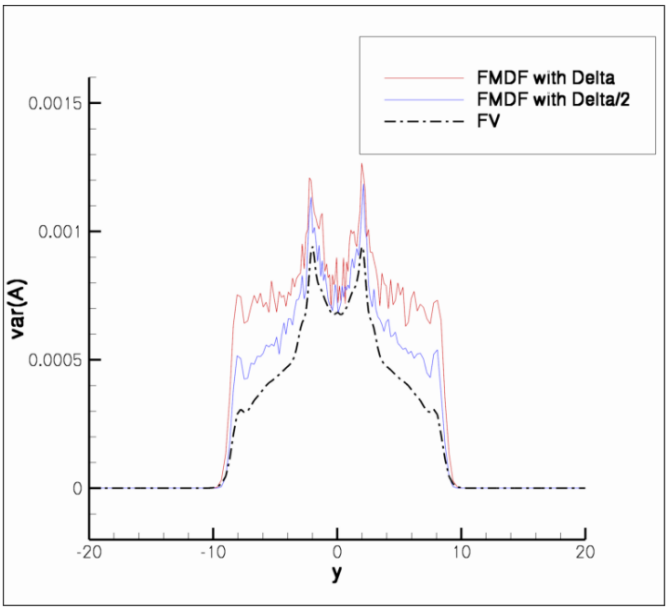

Figure 4.35. Cross-stream variation of the Reynolds averaged SGS variance for the compressible mixing layer at $t = 160$. Red line SFMDF with $\Delta_E = \Delta$, blue line SFMDF with $\Delta_E = 1/2\Delta$, black line FV.

4.4.1 Three-dimensional planar wake

As a further demonstration of the consistency between the SFMDF and the FV, the results for a three-dimensional, planar wake with variable density are presented in this section. This simulation also demonstrates the correct implementation of the inflow/outflow particle boundary conditions as well as the scalability of the SFMDF-MC solver for problems of considerable size. The cross-stream contour plot of the vorticity magnitude (Fig. 4.36) shows a typical Karman vortex street in which vortices pair and roll up, and after which three-dimensional instability ensues resulting in breakdown of regular vortices. The time-averaged temperature distributions of Fig. 4.37 and Fig. 4.38 show that between $x/D = 2$ and $x/D = 4$ transport is primarily due to diffusion, while between $x/D = 4$ and $x/D = 8$ large scale convective transport becomes significant. In addition Fig. 4.38 shows a comparison between the Spalart-Allmaras and the MKEV turbulence models. The temperature decay, and therefore the turbulent mixing, is slightly increased when the MKEV model is used.

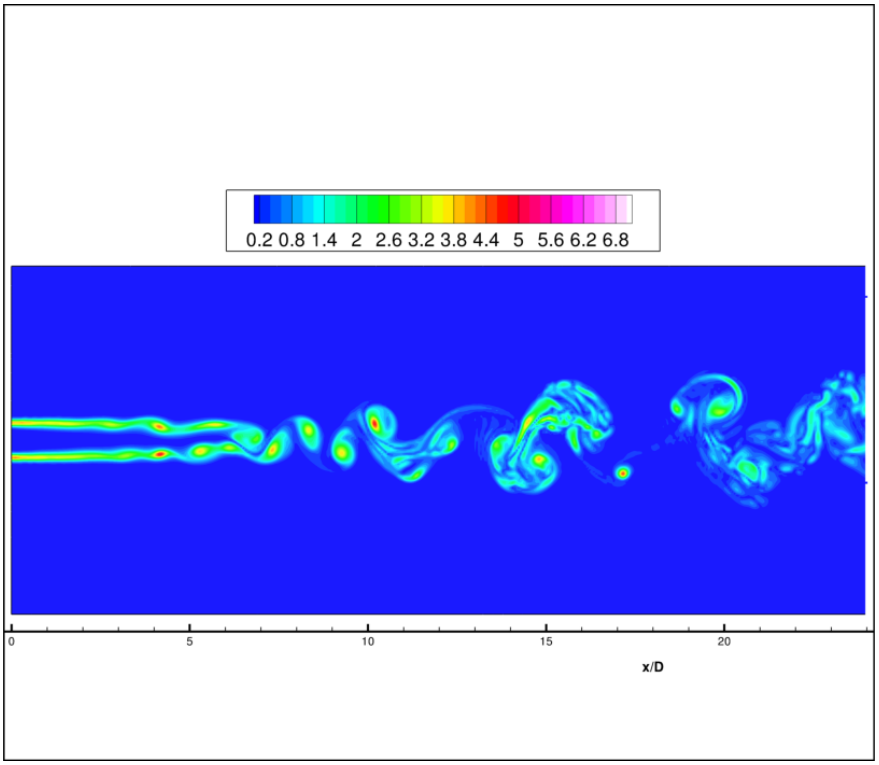

Figure 4.36. Cross-stream (z=0) vorticity magnitude at t=80.

First, the iso-surface 3D plots of the mass fraction of the conserved scalar are shown in Fig. 4.39. The excellent agreement between the two solutions is also evident from the top view of Fig. 4.40, which also show the high degree of three-dimensionality of this flow.

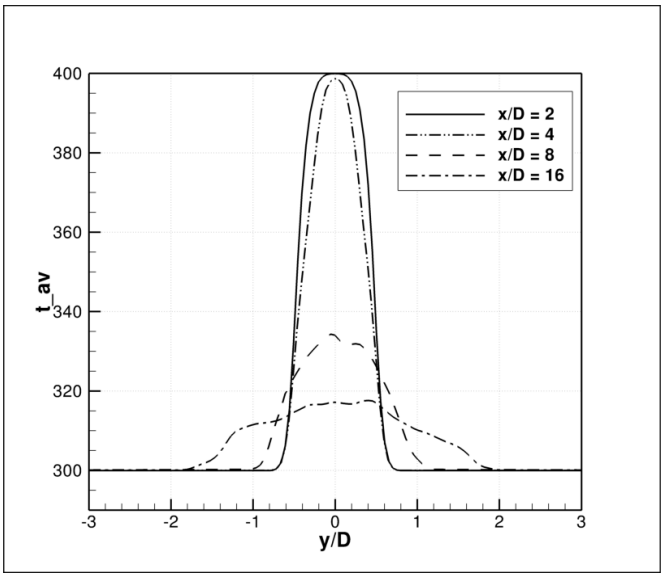

Figure 4.37. Time-averaged temperature at different streamwise locations (t=80).

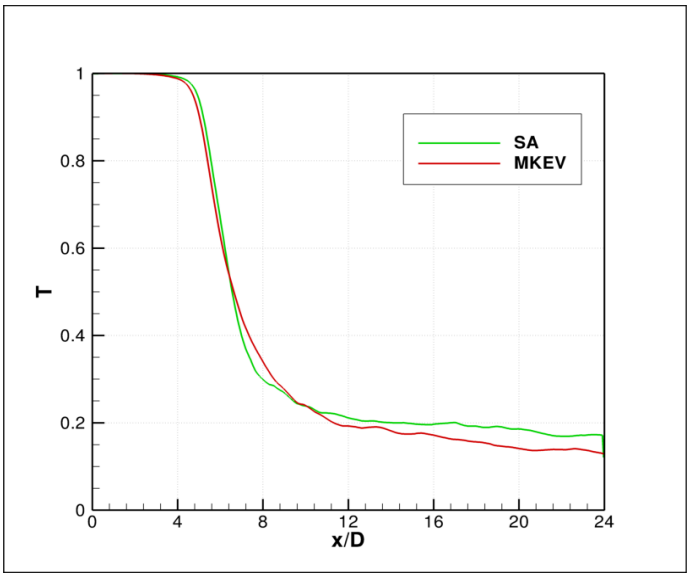

Figure 4.38. Time-averaged temperature along the centerline at t=80. In this plot the temperature is non-dimensionalized as $\overline{T} = (T_0 - T_{\text{inf}})/100$.

Consistency is further demonstrated by Fig. 4.41 and Fig. 4.42, which show the contour of the cross stream temperature and the scatter plot, respectively.

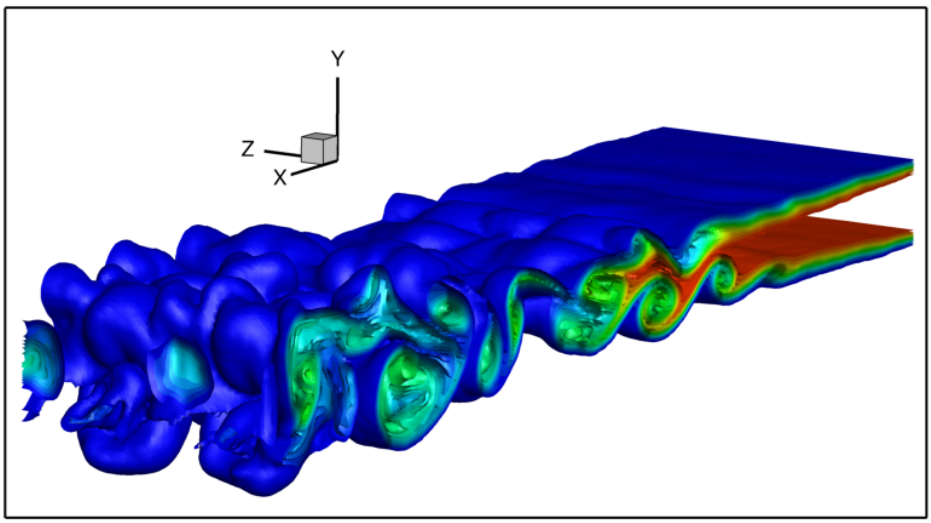

(a)

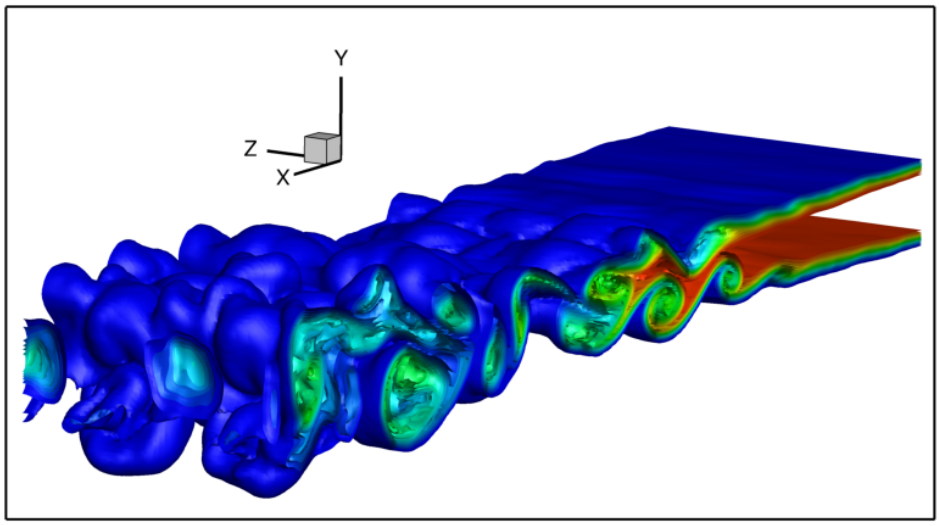

(b)

Figure 4.39. Mass fraction of the conserved scalar at t=80. (a) SFMDF, (b) FV

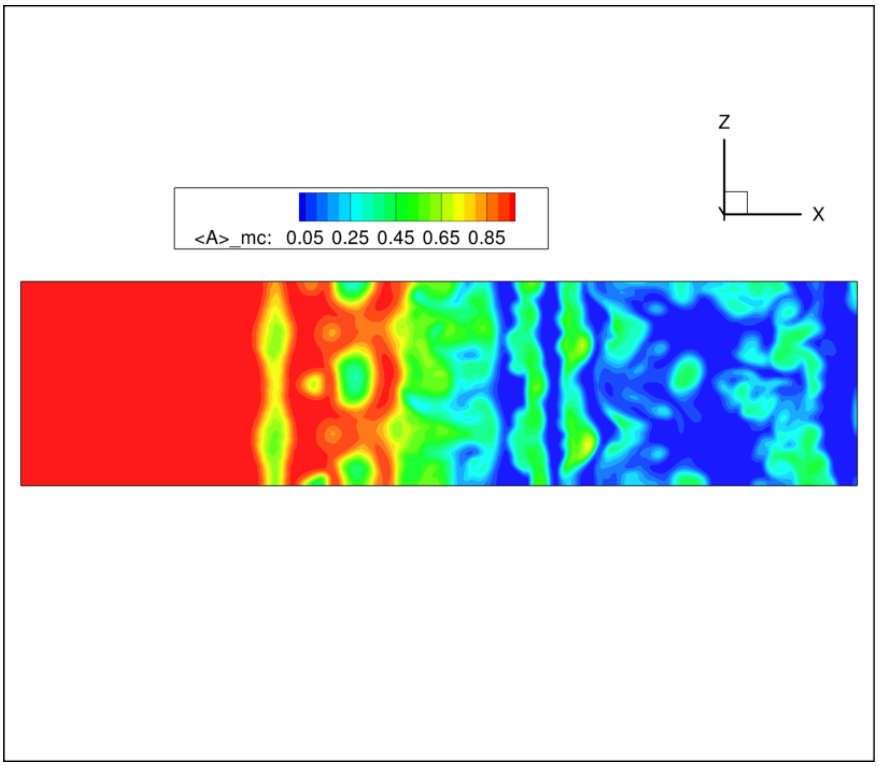

(a)

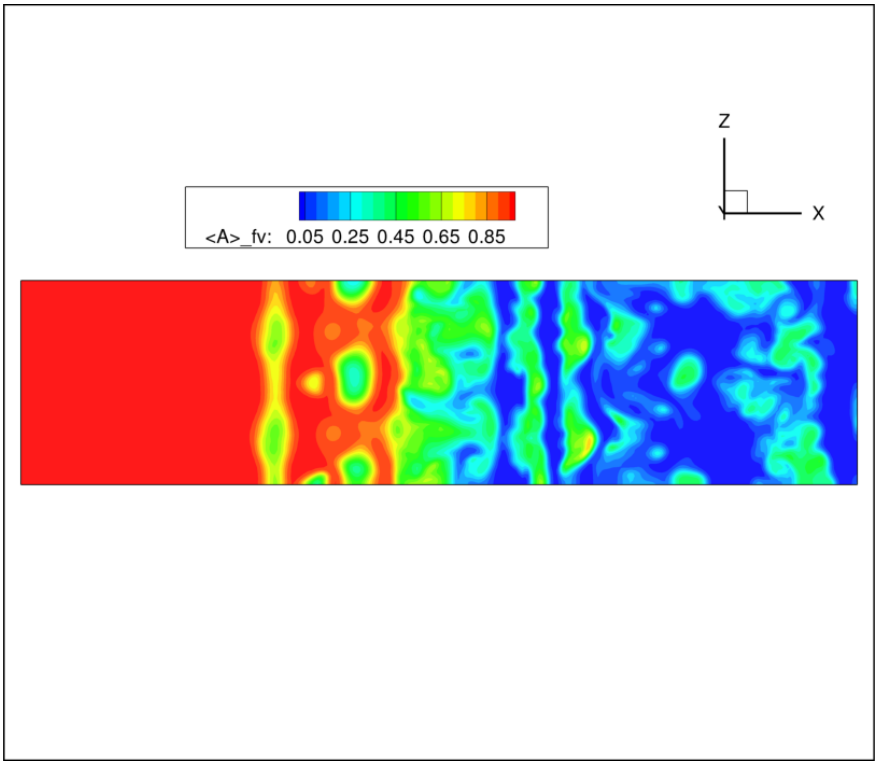

(b)

Figure 4.40. Top view (z=0) of the mass fraction of the conserved scalar at t=50. (a) SFMDF, (b) FV

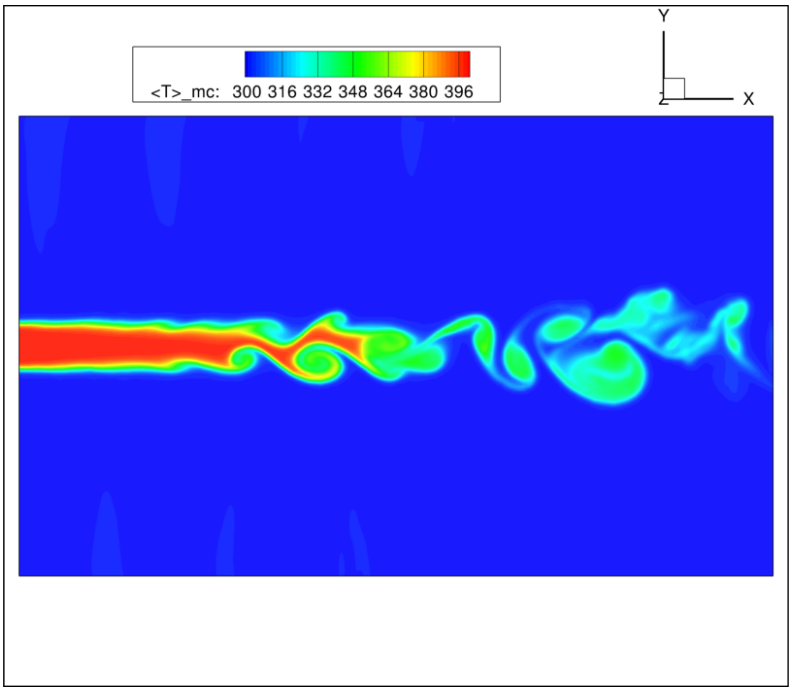

(a)

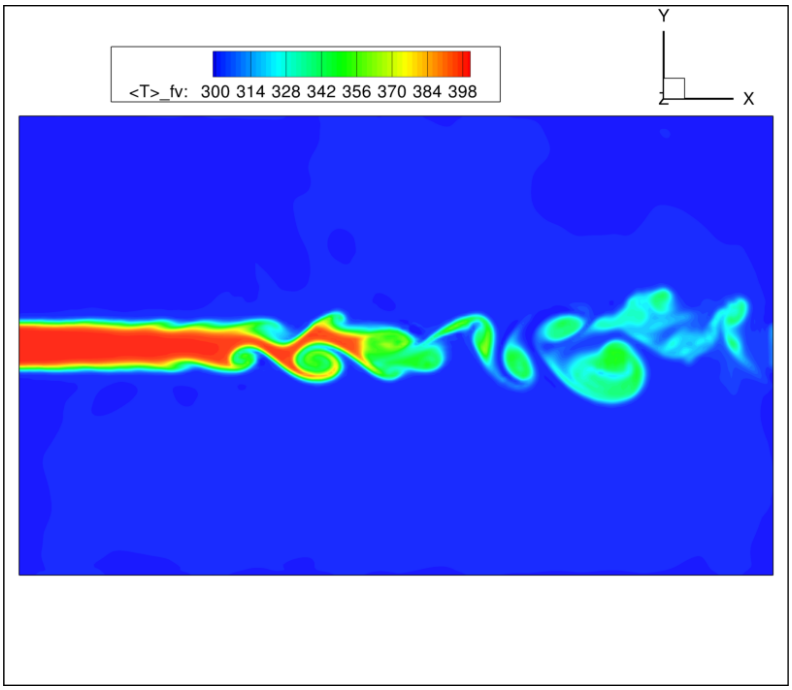

(b)

Figure 4.41. Cross stream contour plots of the filtered temperature at t=50. (a) SFMDF, (b) FV

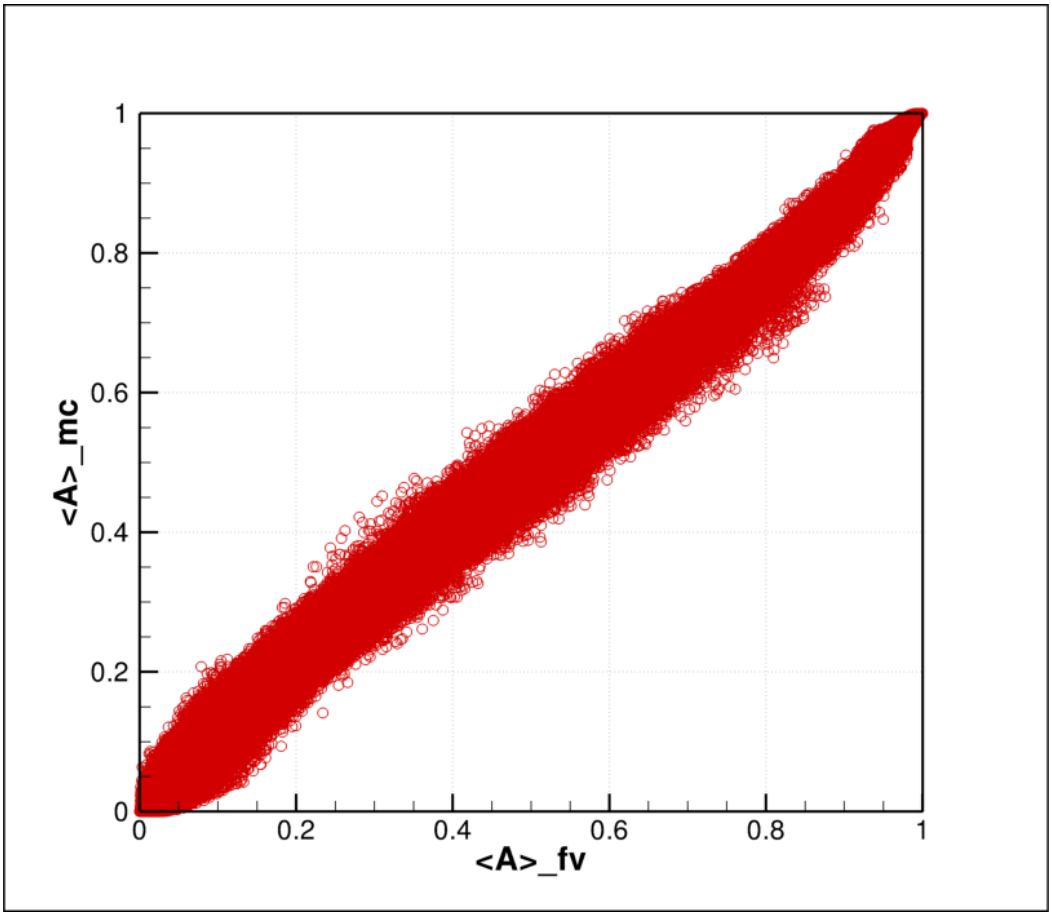

Figure 4.42. Scatter plot of the scalar filtered mass fraction at t=50.

4.5 Computational Requirements

During the development of the Monte Carlo solver more emphasis was placed on robustness rather than optimization. Nevertheless, our results on the CPU times required to carry out a simulation are encouraging. All the tests were performed on the three-dimensional temporal mixing layer with two different grid sizes and three different intitial number of particles per cell (NPC). The results are shown as the percentage increase in CPU time of the hybrid LES-MC simulations over the LES simulation alone.

Grid	NPC	Total number of particles	Increase in CPU time (%)
$32 \times 32 \times 32$	60	1.9 million	26.5
$32 \times 32 \times 32$	120	3.9 million	73.7
$32 \times 32 \times 32$	240	7.8 million	266
$64 \times 64 \times 64$	120	31.4 million	317.4
$64 \times 64 \times 64$	480	125.8 million	1083

Table 4.1. Increase in CPU time when the Monte Carlo module is activated as compared to a standard FV simulation for different grid sizes and initial number of particles (NPC).

As the table shows, when 60 particles per cell are used, the computational overhead of the Monte Carlo solver is less than 30 %. It must be noted that most simulations SMFDF simulations in the literature use around 40 particles per cell. As expected, the CPU times drastically increases when NPC is over 120.
The simulations on the 32^3 grids were carried out using 16 processors, while for the 64^3 grid 64 processors were utilized.
The 3D planar wake case was run on a 3.5 million element grid with 60 initial number of particles per cell, totalling 219 initial million particles. After the initial transient, the average number of particles in the domain reduced to about 195 million. The total run time was 7 hours on 192 cores. This represents an increase of 290 % in computational time for the hybrid scheme as compared to running a pure LES.

Chapter 5

Summary and Future Work

The Scalar Filtered Mass Density Function (SFMDF) method has been implemented on a Three-Dimensional fully Unstructured Parallel Finite Volume Fluid Dynamic solver (US3D), with the goal of improving the accuracy of Large Eddy Simulations of chemically reactive flows.
The SFMDF method was developed in the late '90 and, since then, it has been primarily used for low speed (incompressible) LES of chemically reacting flows on structured grids with a good degree of success. The primary advantage of the SFMDF is that the effect of the sub grid scale (SGS) chemical reaction appears in a closed form and does not require modelling.
This work lay the foundation for the use of the SFMDF methodology on high-speed compressible flows and complex geometries.
First we describe the mathematical formulation of the SFMDF and derive the SFMDF transport equation. The unclosed terms in this equation are identified and modelled. Due to high-dimensionality of the SFMDF transport equation, conventional numerical methods like finite difference or finite volume are impractical to use for its solution. Instead, the concept of equivalent systems is employed. The SFMDF is represented by an ensemble of stochastic particles that, when when their dynamics is simulated by means of the generalized diffusion process, yield the same statistics as the original fluid particles. Numerically, the equivalent stochastic system is solved using a Lagrangian Monte Carlo (MC) method. The SFMDF only represents the transport equation for the scalars (species mass fraction and enthalpy) and, to obtain a solution of the full Navier-Stokes system of equations, it needs to be coupled with a Fluid Dynamic solver that provides, at minimum, the velocity, the pressure and the eddy viscosity fields. This methodology of solving the governing equations is referred to as "hybrid".
Next the Lagrangian Monte Carlo solver that we developed for this work is described in greater detail together with the procedure it was employed to couple it with the existing US3D parallel fluid solver. Both codes share the same data structure and that required the development of routines to track the particles on 3D unstructured grids, to assign the boundary conditions and to efficiently exchange the particles among processors.
Some consistency tests that have been run to validate the SFMDF-MC results. These

tests calculate the first two moments with the SFMDF-MC methodology and compare the results obtained by solving the transport equations for the same quantities with the conventional Finite Volume solver. To facilitate the comparison, only non-reacting flows were considered. The flows simulated are a two-dimensional and a three-dimensional temporal developing mixing layers. The results show that the first moment (mean) of the scalar (species mass fraction or temperature) is pretty insensitive to the numerical parameters and the agreement with the FV results is always very good. On the contrary, the higher moments, and especially the SGS variance, were found to be very sensitive to the grid resolution, the turbulence model and the ensemble domain size. Furthermore the discrepancy between the SFMDF and the FV results increases as the Reynolds number is increased. This was only partially mitigated by the use of the Modified Kinetic Energy Viscosity (MKEV) turbulence model. The reason for this behaviour are not clear. The initial number of particles per cell used in the simulation was not found to influence the accuracy of the results.

Results for variable-density flows are also presented, in which a low Mach number mixing layer is initialized with different densities on the upper and lower streams. The comparison with the filtered temperature calculated from the FV and the SFMDF solver is very good, both for the instantaneously results and for the Reynolds averaged ones. The particle density, obtained by summing the particle weights inside the ensemble domain, also agrees well with the FV results, although it shows some noise due to statistical error.

Some simulations has also been carried out for a compressible mixing layer at $M_c = 0.8$. The results, although preliminary, show that the SFMDF method is capable of dealing with compressible features like a shock waves. More simulations are still needed in order to assess the validity of neglecting the SGS pressure terms in the enthalpy equation for high speed flows.

Although the SFMDF-MC methodology is computationally more expensive than a conventional LES, it was shown that, in our implementation, this computational overhead is still acceptable even when using a very large number of particles. These results make the SFMDF-MC methodology a viable candidate to use for practical combustion system where DNS is not feasible.

It must be emphasized that the objective of this work is to lay the foundations for the use of the SFMDF-MC methodology in conjunction with high-order, fully unstructured compressible solver. This will enable, in the very near future, the study of high-speed, chemically reacting flows inside complex geometries as in a supersonic RAMJET. The results, therefore, are only preliminary and focus prevalently on the validation of the SFMDF-MC solver developed.

The next steps in the development process coluld be to run a reactive mixing layer and validate the results against DNS data. After that more complex simulations, e.g. jet or wake flows, could be attempted and the results validated against experimental data. Furthermore, it will be interesting to see the performance of the SFMDF-MC methodology in wall-bounded flows. It is well know that chemical reactions play an important role in boundary layer separation and the use SFMDF-MC has the potential of greatly improve the accuracy of these simulations.

Bibliography

[1] Poinsot, T., and Veynante, D., *Theoretical and Numerical Combustion*, R.T. Edwards, Philadelphia (2001).

[2] Pope, S. B., *Turbulent Flows*, Cambridge Univ. Press, Cambridge, England, U.K., (2000).

[3] Peterson D. M. and Candler, G.V., *Hybrid Reynolds-Averaged and Large-Eddy Simulation of Normal Injection into a Supersonic Crossflow*, Journal of Propulsion and Power, Vol. 26, No. 3, (2010), pp. 533–544.

[4] Williams, F. A., *Combustion Theory, 2nd ed.*, Benjamin/Cummings, Menlo Park, CA, (1985).

[5] Pope, S., B., *Computations of Turbulent Combustions: Progress and Challenges*, Proceedings of the Combustion Institute, Vol. 23, No. 1, (1990), p. 591–612.

[6] Madnia, C., K., and Givi, P., *Direct Numerical Simulation and Large Eddy Simulation of Reacting Homogeneous Turbulence*, In Galperin and Orszag, (1993), p. 315–346.

[7] Eidson T. M., *Numerical Simulation of the Turbulent Rayleigh-Benard Problem using Subgrid Modeling*, J. Fluid Mech., Vol. 158 (1985) p. 245–268.

[8] Pino Martin M., et al., *Subgrid Scale Models for Compressible Large Eddy Simulations*, Theoret. Comput. Fluid Dynamics (2000) 13: p. 361-376.

[9] Knight, D., et al., *Compressible large eddy simulation using unstructured grids*, AIAA Paper 98-0535, (1998).

[10] Bardina, J., et al., *Improved Turbulence Models based on Large Eddy Simulations of Homogeneous, Incompressible, Turbulent Flows*, Department of Mechanical Engineering Report TF-19, Stanford University, CA. (1983).

[11] Spalart, P., R., and Allmaras, S., R., *A One-Equation Turbulence Model For Aerodynamic Flows*, AIAA paper 1992-0439, (1992).

[12] Pope, S., B., *PDF Methods for Turbulent Reactive Flows*, Progress in Energy and Combustion Sciences, Vol. 11, No. 2, (1985) p. 119–192.

[13] Colucci, P., J., *Large Eddy Simulation of Turbulent Reactive Flows: Stochastic Representation of the Subgrid Scale Scalar Fluctuations*, PhD Thesis, State University of New York at Buffalo (1998).

[14] Colucci P. J., Jaberi F. A., and Givi P., *Filtered Density Function for Large Eddy Simulation of Turbulent Reacting Flows*, Physics of Fluids, (1998) Vol. 10, No. 2, pp. 499–515.

[15] Banaeizadeh, A., et al., *Compressible Scalar Filtered Mass Density Function Model for High-Speed Turbulent Flows*, AIAA Journal, Vol. 49, No. 10, (2011) p. 2130–2142.

[16] Jaberi, F., A., et al., *Filtered Mass Density Function for Large-Eddy Simulation of Turbulent Reacting Flows*, J. Fluid Mech. (1999), vol. 401, p. 85–121.

[17] N. Ansari, G., M., et al., *Filtered density function simulator on unstructured meshes*, J. Comp. Phys., (2011), 230, p. 7132–7150.

[18] Fox, O., R., *Computational Models for Turbulent Reactive Flows*, Cambridge University Press, (2003).

[19] Nompelis, I., et al., *Development of a Hybrid Unstructured Implicit Solver for the Simulation of Reacting Flows Over Complex Geometries*, AIAA 2004-2227, (2004).

[20] Nompelis, I., Drayne T., and Candler, G., V., *A Parallel Unstructured Implicit Solver for Hypersonic Reacting Flow Simulations*, AIAA Paper 2005-4867, (2007).

[21] MacCormack, R.W. and Candler, G.V., *The Solution of the Navier-Stokes Equations Using Gauss-Seidel Line Relaxation*, Computers and Fluids, Vol. 17, No. 1, (1989), pp. 135–150.

[22] Candler, G.V. and MacCormack, R.W., *The Computation of Hypersonic Ionized Flows in Chemical and Thermal Nonequilibrium*, Journal of Thermophysics and Heat Transfer, Vol. 5, No. 3, (1991), pp. 266–273.

[23] Bartkowicz, M., et al., *Numerical Simulations of Roughness Induced Instability in the Purdue Mach 6 Wind Tunnel*, AIAA AIAA-2010-4723, (2010).

[24] Mavriplis D. J., *Revisiting the Least-Squares Procedure for Gradient Reconstruction on Unstructured Meshes*, NASA Report CR-2003-212683, (2003).

[25] Karypis, G., and Kumar, V., *Unstructured Graph Partitioning and Sparse Matrix Ordering System*, http://www.cs.umn.edu/ metis, (1998).

[26] Subramaniam, S. and Haworth, D.C., *A probability density function mathod for turbulent mixing and combustion on three-dimensional unstructured deforming meshes*, Int J Engine Research, Vol. 1, No. 2, (2000) pp. 171–190.

[27] Jou, W., H., et Riley, J., J., *Progress in Direct Numerical Simulations of Turbulent Reacting Flows*, AIAA Journal, Vol. 27, (1989) p. 1543–1556.

[28] Yilmaz, S., L., *RANS/PDF and LES/FDF for Prediction of Turbulent Premixed Flames*, PhD Thesis, University of Pittsburgh, (2008).

[29] Givi P., *Model Free Simulations of Turbulent Reactive Flows*, Prog. Energy Combust. Sci., Vol. 15, (1989) p. 1–107.

[30] Vreman, B., Geurts, B., and Kuerten, H., *Realizability Conditions for the Turbulent Stress Tensor in Large-Eddy Simulation*, J. Fluid Mech., Vol. 278, (1994) p. 351–362.

[31] Vreman B., *Direct and Large-Eddy Simulation of the Compressible Turbulent Mixing Layer*, Ph.D. Dissertation, University of Twente, Enschede, The Netherlands, (1995).

[32] Yee, H. C., Vinokur M. and Djomehri M. J., *Entropy Splitting and Numerical Dissipation*, J. of Comp. Physics, Vol. 162, (2000) p. 33–81.

[33] Sjoogreen, j., and Yee, H. C., *Multiresolution Wavelet Based Adaptive Numerical Dissipation Control for High Order Methods*, J. of Scient. Computing, Vol. 20, No. 2,(2004) p. 211–255.

[34] Aldama, A.,A., *Filtering Techniques for Turbulent Flows Simulations*, Lecture Notes in Engineering, Vol. 49, (1990), Springer-Verlag, New York, NY.